

The Virtual Quantum Device (VQD): A tool for detailed emulation of quantum computers

Cica Gustiani¹, Tyson Jones^{1,2}, and Simon C. Benjamin^{1,2}

¹Department of Materials, University of Oxford, Parks Road, Oxford OX1 3PH, United Kingdom

²Quantum Motion, 9 Sterling Way, London N7 9HJ, United Kingdom

We present the Virtual Quantum Device (VQD) platform, a system based on the QuEST quantum emulator. Through the use of VQDs, non-expert users can emulate specific quantum computers with detailed error models, bespoke gate sets and connectivities. The platform boasts an intuitive interface, powerful visualisation, and compatibility with high-performance computation for effective testing and optimisation of complex quantum algorithms or ideas across a range of quantum computing hardware. We create and explore five families of VQDs corresponding to trapped ions, nitrogen-vacancy-centres, neutral atom arrays, silicon quantum dot spins, and superconducting devices. Each is highly configurable through a set of tailored parameters. We showcase the key characteristics of each virtual device, providing practical examples of the tool's usefulness and highlighting each device's specific attributes. By offering user-friendly encapsulated descriptions of diverse quantum hardware, the VQD platform offers researchers the ability to rapidly explore algorithms and protocols in a realistic setting; meanwhile hardware experts can create their own VQDs to compare with their experiments.

1 Introduction

In this paper we introduce the Virtual Quantum Device (VQD) platform, a system for emulating noisy quantum computers. The VQD supports realistic error models and bespoke opera-

tions with the flexibility to tailor to the diverse range of quantum hardware currently being investigated worldwide. Alongside the VQD platform itself, we have worked with collaborators to establish the following VQD instances: multi-node ion traps, nitrogen-vacancy-centre (NV-centre) diamond qubits, neutral atoms, silicon qubits, and superconducting qubits.

The VQD platform is built atop QuESTlink [43], a Mathematica extension of QuEST [44], itself an open-source emulator of quantum computers developed in C and C++. A user can access these tools through a Mathematica notebook with the appropriate licence, or through the Wolfram Engine which is presently free for developers. QuESTlink combines Mathematica's powerful symbolic operations with QuEST's high-performance backend, enabling virtual devices to be highly configurable through an intuitive interface, and able to leverage powerful visualisation facilities, without compromising performance. Through the VQD platform, researchers can effectively test and optimise complex quantum algorithms or ideas across a range of quantum computing architectures. In its current form, the QuESTlink tool's capability to exactly model a system of qubits is limited only by the host computer's memory. For example a 64 GiB RAM system can emulate up to 32 qubits in double precision, or about half as many if one uses the full density matrix representation rather than state vectors ¹. As we presently explain, the VQD platform is flexible with respect to this choice.

In the VQD platform, end-users can easily select the particular, pre-existing VQD that they wish to emulate (a given form of ion trap, for ex-

¹In future, QuESTlink may be deployed in distributed settings, as already supported by the underlying QuEST simulator.

Cica Gustiani: cicagustiani@gmail.com

Simon C. Benjamin: simon.benjamin@materials.ox.ac.uk

arXiv:2306.07342v4 [quant-ph] 16 Feb 2025

ample). Users can re-configure an instance of a virtual device by adjusting a set of parameters that are tailored to each type of device; some of these parameters will be immediately comprehensible to a non-expert user. Other parameters are provided for the more expert users to adjust if they wish. The parameters are carefully chosen to capture the main characteristics and describe the critical error sources of the device. For instance, the parameters may include the number of qubits and nodes, atom locations, relaxation times T_1 and T_2 , qubit frequencies, gate fidelities, Rabi frequencies, and more. Ultimately of course a user can create their own VQD as a variant of one of the existing devices or as a wholly new class of system. Thus, for example, a research team who have developed a specific type of device might do this in order to allow others to experiment on their system *virtually* and find interesting tasks for it – or simply as an internal tool to closely model their experiments.

To ensure an accurate and realistic simulation, the virtual device is designed to reflect a close approximation to the physical reality by only providing access to physically possible native operations. For example, in the case of neutral atoms, multi-qubit gates can only be implemented when the atoms are within the overlapping blockade radii. The corresponding VQD tracks the atom’s spatial configurations and movements, to ensure that the operations called for by a user are physically possible.

Typically the user will input a quantum circuit composed of legitimate operations, and the tool can output the noise-decorated circuits according to the instantiated virtual device, as well as the final state of the virtual device, such as the final arrangement of atoms in neutral atom architectures.

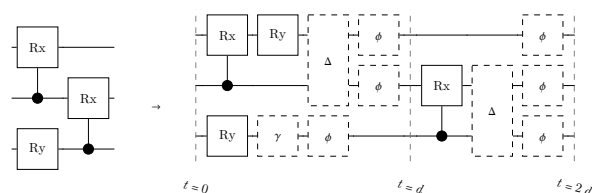
This paper presents several demonstrations utilising the VQD platform which highlight the unique features of each qubit implementation. These demonstrations serve as practical examples of the tool’s usefulness and exhibit the specific attributes of each device. For instance, the demonstration of entanglement distillation on trapped ions showcases the long coherence times and precise laser control capabilities of these qubits. The simulation of BSC theory on diamond NV-centers emphasises the central spin system connectivity of these qubits. The demonstration of graph state

preparation on neutral atoms highlights the mobility and two-dimensional connectivity of these qubits. By reproducing the published experiment results involving Bell state preparation on silicon qubits, we demonstrate that our error model accurately captures the device. Lastly, the variational algorithm demonstration on superconducting qubits highlights the potential for these qubits to implement complex algorithms as well as the importance of tailoring circuits to the system’s connectivity.

The VQD code is readily accessible for use here [32]. Currently in its inaugural beta stage, the code is fully functional and can be employed to reproduce the results presented in this paper. It is important to note that while this version is operational, it is not the final form. Future versions will reflect iterative enhancements and refinements. This presents a unique opportunity for users to engage with the code in its developing stages while being capable of effectively using the functionalities presented here.

2 The virtual quantum device package

A virtual quantum device provides a layer of abstraction above QuESTlink’s *device specification* facility introduced in version 0.6 [43]. The latter is a static description of how a realistic, error-prone and constrained quantum device might realise an intended unitary circuit; through a proximate channel composed of mixing operators and a potentially distinct set of unitary operators. For instance, consider how a simple 3-qubit 3-gate circuit might be affected on a noisy device.



Specifically, the device imperfections in this example are such that gates on the bottom qubit induce damping (signified by γ), those on the bottom and middle induce depolarising (Δ), and upon the top two induce depolarising and an erroneous rotation about the Y axis. All idle qubits experience dephasing noise (ϕ) while waiting for the slowest operation in their automatically scheduled parallel batch (in the first round;

with duration d). Upon a given input state, the right-hand-side channel may be simulated through the density matrix formalism to completely determine the *noisy*, the real-world output of the ideal left circuit.

In this way, a device specification offers a mapping between ideal unitary circuits and realistic channels admitted by the modelled hardware device. Device specifications include provisions of active and passive noise behaviour, restricted gate sets and qubit topologies, gate substitutions, durations and scheduling, time-dependent noise, general variable-dependent noise (such that noise severity may depend on preceding operations) and *hidden qubits* to model dynamics outside the computational state space. Given a collection of pre-made specifications, they permit a user to rapidly study the differing behaviours of realistic quantum computers when tasked with executing the same circuit.

While simple and powerful to *users* of a device specification, *producing* a specification (as per the guide here [42]) has several potential pain points. In [Appendix A](#) we describe these challenges, and how they motivated the choice of QuESTlink as the platform upon which to build the VQD framework. There we explain that QuESTlink’s unique combination of a well-featured emulator (QuEST) with Mathematica as a powerful – albeit commercial – symbolic manipulation tool, provided elegant design solutions to some rather complex challenges.

A particular feature of QuESTlink which we stress here is its capability to switch between state vector and density matrix representations. The latter can comprehensively represent the impact of noise processes on a quantum state, and QuESTlink supports general Kraus operators acting on the density matrix to fully encode those processes. However the representation is quadratically more expensive than statevector simulation of the original noise-free circuit, and this is sometimes prohibitive. Fortunately, these steeper memory and time costs can often be avoided by the user instead opting for Monte Carlo statevector simulation, whereby expected values of the VQD prescribed noisy quantum states are evaluated through repeated sampling of an ensemble of error-affected statevectors [31]. QuESTlink’s `SampleExpecPauliString` function pseudo-randomly replaces each decoherence

channel with an operator from its Kraus map, and acts it upon a statevector before computing the expected value. This process is repeated until the average of the samples converges. Thus, while virtual quantum devices are typically specified in terms of operations that are incompatible with the state vector representation, and indeed the full density matrix representation is available, a user can opt to *automatically translate* the emulation task into the Monte Carlo paradigm. This often enables simulation of realistic noisy devices at modest memory costs.

3 Error models

In this section, we elaborate the error models and forms of noise considered in our virtual devices. Each noise model can be described using Kraus maps and classical descriptions. Kraus maps mathematically describe the evolution of quantum states resulting from interactions with the environment, while classical descriptions incorporate errors that can be observed in real-life situations. For instance, in neutral atoms, the atoms can be completely ejected into the environment. Such a situation can be straightforwardly indicated by suitable flags.

By combining these approaches, we provide a tool with a sophisticated error model that is powerful but with a friendly user interface. This enables us to easily simulate and analyse various scenarios or quantum algorithms on virtual qubits, with accurate descriptions of the effects of noise and other error sources. It is important to note that our models do include some basic simplifications with respect to what occurs in real experiments; we have made each of our demonstration VQDs sufficiently complex to capture much of the uniqueness of each platform, but there are many respects in which they can be made more sophisticated by a user who is expert in the relevant system. In the following, we outline the simplifying assumptions that apply to our demonstration virtual devices.

Firstly, each operator acting on a qubit is subjected to the rotating-wave approximation implemented within its own rotating frame of reference; thus, in the absence of any gate application or noise, the qubit simply undergoes the identity operation. Secondly, when the user provides the T_2 time, our default assumption is that any re-

quired Hahn-echo or dynamical decoupling is understood to be applied ‘in the background’ to the passive qubits – that is to say, such decompiling is not explicitly generated in the circuits produced by the VQD platform. Lastly, it is important to recognise that the QuEST family of tools is designed to represent only discrete events occurring to a series of qubits – thus other tools must be used to, e.g., model the continuous-time dynamics of an n -level system subject to given Hamiltonian pulse. (However, having understood the effect of that pulse within a pair of levels deemed to constitute a qubit, then the resulting unitary or non-unitary operation can certainly be described within a VQD.)

A final remark is that the density matrices presented in this paper (e.g., [Figures 3](#) and [16](#)) are visualisations generated directly from the density matrix representation in the VQD tool and are not modified to account for any imperfections in experimental tomography.

3.1 Standard forms of noise

We begin by describing textbook standard forms of noise for one- and two-qubit gates. They include one- and two-qubit depolarising and dephasing and one-qubit amplitude damping. While the VQD platform supports the use of arbitrary Kraus maps to represent general non-unitary processes, these three particular forms of noise are so common that it is useful to overtly specify their implementation within the VQD (and indeed, there are optimised algorithms for implementing these specific forms of noise within the underlying QuEST tools).

Depolarising and dephasing channels are typically attributed to gate noise. Amplitude damping channel is often attributed to noise in initialisations and measurement processes, or to continuous relaxation of passive qubits. These forms of noise are straightforward to implement yet powerful in describing various error processes happening in the experiments. Note that the quantum channels below can be viewed as completely positive trace-preserving (CPTP) maps.

In the following, we denote ρ as a quantum state, p as the error parameter, and $\sigma \in \{X, Y, Z\}$ are Pauli operators. The *one-qubit depolarising channel* on qubit j ($depol_j$) maps

$$\rho \mapsto (1-p)\rho + \frac{p}{3} \sum_{\sigma} \sigma_j \rho \sigma_j, \quad (1)$$

where $p \in [0, \frac{3}{4}]$. The *two-qubit depolarising channel* acts homogeneously on qubits i and j ($depol_{i,j}$), and maps

$$\rho \mapsto (1-p)\rho + \frac{p}{15} \left(\sum_{\sigma} \sigma_i \rho \sigma_i + \sum_{\sigma} \sigma_j \rho \sigma_j + \sum_{\sigma\sigma'} \sigma_i \sigma'_j \rho \sigma_i \sigma'_j \right), \quad (2)$$

where $p \in [0, \frac{15}{16}]$. The *one-qubit dephasing channel* acts on qubit j ($deph_j$) and maps

$$\rho \mapsto (1-p)\rho + pZ_j \rho Z_j, \quad (3)$$

where $p \in [0, \frac{1}{2}]$. The *two-qubit dephasing channel* acts homogeneously on qubits i and j ($deph_{i,j}$) and maps

$$\rho \mapsto (1-p)\rho + \frac{p}{3} (Z_i \rho Z_i + Z_j \rho Z_j + Z_i Z_j \rho Z_i Z_j), \quad (4)$$

where $p \in [0, \frac{3}{4}]$.

The *amplitude damping channel* on qubit j (amp_j) corresponds to the error map

$$\rho \mapsto \sum_A A_j \rho A_j^\dagger, A \in \left\{ \begin{pmatrix} 1 & 0 \\ 0 & \sqrt{1-p} \end{pmatrix}, \begin{pmatrix} 0 & \sqrt{p} \\ 0 & 0 \end{pmatrix} \right\}, \quad (5)$$

where $p \in [0, 1]$; for the case $p = 1$, the quantum state ρ will be in the state $|0\rangle\langle 0|$.

3.2 Standard error parameter estimate from average gate fidelity

In configuring our virtual quantum devices, we often encounter the situation that the experimental team’s best model for the noise in a given process is of the depolarising and/or dephasing type. We deem an operation to have *standard error* when its noise model can be described by the composition

$$\mathcal{E}(p, q) \equiv deph(p) \circ depol(q) \quad (6)$$

where $depol(p)$ and $deph(q)$ are one- or two-qubit parameterised depolarising and dephasing noise defined in [Section 3.1](#)). It is then very valuable to be able to take fidelity estimates obtained experimentally and translate them into the noise severities p and q . Fortunately, this is straightforward, and the procedure is described in [Appendix B](#).

3.3 Off-resonant Rabi oscillation

Many quantum gate operations are realised by applying a coherent pulse of EM (e.g., microwave)

radiation at a frequency resonant with the energy gap of the qubit. Ideally, the qubit is perfectly isolated during the process in order to prevent the unwanted driving of other qubits. However, as this ideal is generally not achieved, we define the error induced by off-resonant frequency on the

$$\left[\begin{array}{c} \left(\cos\left(\frac{\Omega_R t}{2}\right) - \frac{i\Delta}{\Omega_R} \sin\left(\frac{\Omega_R t}{2}\right) \right) e^{i\Omega_R t/2} \\ - \frac{i\Omega}{\Omega_R} \sin\left(\frac{\Omega_R t}{2}\right) e^{-i\Omega_R t/2} \end{array} \right] \left[\begin{array}{c} - \frac{i\Omega}{\Omega_R} \sin\left(\frac{\Omega_R t}{2}\right) e^{i\Omega_R t/2} \\ \left(\cos\left(\frac{\Omega_R t}{2}\right) + \frac{i\Delta}{\Omega_R} \sin\left(\frac{\Omega_R t}{2}\right) \right) e^{-i\Omega_R t/2} \end{array} \right], \quad (7)$$

where $\Omega_R = \sqrt{\Omega^2 + \Delta^2}$ is the detuned frequency. Equation (7) describes Rabi oscillation of two-level system (states $|0\rangle$ and $|1\rangle$) in the frame of qubit q , such that it approaches identity for a large frequency difference Δ . It is thus desirable for qubits to have significantly diverse Rabi frequencies.

3.4 Crosstalk

An ideal quantum computer would localise gate operations to only the qubits which are nominally involved, and only for the defined duration of the gate. In reality, this localisation may be imperfect either in time (leading to a residual interaction even in the ‘off’ state) or in space whereby ‘bystander’ qubits are brought into the process. Generally, these effects are addressed as *crosstalk*. Two forms of crosstalk occur in the VQDs that we discuss presently.

The first type is in the form of *conditional phase* on bystander qubits, according to the state of a given qubit. This effect may occur only during a gate operation, or it may be a continuous process constituting a failure to decouple the qubits entirely. In either case, we express this error between qubits p and q , in the form of conditional Z -rotation,

$$|0\rangle\langle 0|_p \otimes I_q + |1\rangle\langle 1|_p \otimes Rz(\alpha)_q, \quad (8)$$

or the ZZ -coupling,

$$e^{-i\alpha Z_p Z_q}, \quad (9)$$

where α is the error parameter which may be dependent on the duration of any active gates, the spatial location of bystanders, etc.

The second type is *unwanted exchange interaction*, a commonly encountered crosstalk model that occurs during the operation of a two-qubit

idle qubits during the drive.

Let q be the actively driven qubit with Rabi frequency Ω for a duration t . The passive qubit j with frequency difference Δ receives an off-resonant drive described with the following unitary matrix

gate and results in partial coupling with bystanders. It has the form of

$$e^{-i(X_i X_j + Y_i Y_j + Z_i Z_j)\theta/4}, \quad (10)$$

where the error parameter θ depends on the duration of the operated two-qubit gate.

There are of course many other cross-talk effects, each dependent on the physics of the system. For example, unwanted partial entanglement with bystander qubits, as may occur in laser-driven two qubit ion trap gates [36, 105], has elements in common with the two phenomena described above but is distinct from either. The VQDs we introduce can be extended to accommodate any such effects, by extending and adapting the established examples.

3.5 Passive noise and free induction decay

Within all our VQDs we include a process of *passive noise* i.e., noise operations to which qubits are subjected while they are not actively part of an operation; typically the passive noise has a time parameter corresponding to the duration of the active procedure. Passive noise can have any form within the VQD framework, and can be effectively ‘overwritten’ by processes such as crosstalk that engage the nominally passive qubits with the active ones. However, in several cases the passive noise is of a simple form that captures an isolated qubit’s decay processes.

The coherence time of an individual qubit is commonly characterised by the loss of coherence in the xy -axis (transversal relaxation) and z -axis (longitudinal relaxation). In practice, these characteristics are commonly identified by how long a quantum state can maintain the $|+\rangle$ state for the transversal relaxation and the $|1\rangle$ state for the longitudinal relaxation.

In many systems the more rapid process is the traversal relaxation characterised by T_2 (or T_2^* when there is no mitigating procedure, such as Hahn echo, employed). This decay describes the loss of phase information and ultimately renders a state into a classical mixture of its basis components. In our VQDs we employ to model each with dynamic error parameters growing with time Δt as follows

$$\text{deph} \left(\frac{1}{2} (1 - e^{-\Delta t/T_2}) \right) \quad (11)$$

$$\text{deph} \left(\frac{1}{2} (1 - e^{-(\Delta t/T_2^*)^2}) \right) \quad (12)$$

for the exponential T_2 and the gaussian T_2^* decays, respectively. In practice, the T_2^* is much shorter than the T_2 . The T_2^* characteristic can be “echoed-out” to T_2 by continuously applying Hahn echo pulses to passive qubits; this technique is also known as *dynamical decoupling*. In our models, we typically assume that any such process is applied ‘in the background’ (and imperfections in that process are captured by suitably adjusting the passive noise operations) so that T_2 is the relevant timescale. Nevertheless, certain VQDs have the option of disabling this assumption and thus experiencing the ‘raw’ T_2^* process.

In the majority of qubit platforms, the longitudinal relaxation time T_1 is significantly longer than the T_2 (superconducting qubits being an exception). Depending on the typically observed events, the T_1 decay is approximated with depolarising noise or amplitude damping with error parameters increasing with duration Δt :

$$\text{depol} \left(\frac{3}{4} (1 - e^{-\Delta t/T_1}) \right) \quad (13)$$

$$\text{amp} \left(1 - e^{-\Delta t/T_1} \right) \quad (14)$$

for depolarising and amplitude damping models, respectively. The amplitude damping model is used on systems where the qubits decay to a lower energy state (that defines $|0\rangle$) after the T_1 time. The depolarising error is used when the qubits are completely mixed after the T_1 time.

3.6 SPAM errors

State preparation and measurement (SPAM) involve similar processes for many systems. In

many cases, the same error characteristic constitutes state preparation and qubit readout processes. Typical SPAM error models involve amplitude damping and bit-flip errors.

The amplitude damping (Equation (5)) characterises asymmetric error that favours one of the states. For instance, readouts that involve detecting photons, in which photon loss is more probable than dark counting.

On the other hand, bit-flip noise captures error that happens symmetrically, which is described with random X application

$$\rho \mapsto (1 - b)\rho + bX\rho X, \quad (15)$$

where $b \in [0, 0.5]$ is the probability of the error to occur – notice that $b = 0.5$ is the most severe noise, since $b = 1$ would correspond to a definite, and therefore perfectly correctable, X operation. On two-qubit measurements such as parity measurement on a pair of silicon spin qubits, bit-flip error may be equally probable to happen to either or both qubits. The two-qubit bit-flip noise on qubits i, j has the following map

$$\rho \mapsto (1 - b)\rho + \frac{b}{3}(X_i\rho X_i + X_j\rho X_j + X_i X_j \rho X_i X_j), \quad (16)$$

where $b \in [0, 0.75]$ is the meaningful range of probability for an error to occur.

We emphasise that the above models are merely examples that occur so frequently that it is useful to name and define them; the VQD platform supports completely arbitrary forms of passive noise. Indeed one can opt to set passive noise to zero, and instead include in the definition of each active operation a complete description of the implications for all qubits.

3.7 Leakage and Loss errors

In many systems, the two levels deemed to be the qubit $|0\rangle$ and $|1\rangle$ are merely selected states within a large set of physical states of the physical entity representing the qubit. Restricting the entity to the $\{|0\rangle, |1\rangle\}$ subspace may be challenging and imperfectly achieved. The resulting “leakage errors” errors correspond to the qubits escaping to a higher level. Alternatively, a “loss error” corresponds to the qubit-representing entity even physically disappearing – for example, a photonic qubit being absorbed within a fibre, or an atom escaping from its trap.

One can consider three types of scenarios. Firstly, when the qubit is partially leaked to the environment and thus cannot be recovered. This error is described with a non-trace preserving map. For instance, implementing multi-qubit gates in neutral atoms involves exciting the corresponding atom(s) to a high-level Rydberg state followed by relaxation to the ground state with a high probability. Since the ground state encodes a qubit state, other relaxation scenarios imply that the qubit remains outside the computational basis. Secondly, when the qubit is physically ejected from the system. This error is captured with a classical parameter — whether the qubit is present or absent. Lastly, a leakage that commonly occurs in solid-state qubits, where it leaks to a higher level and can potentially be recovered. However, in the VQD specifications discussed here, this event is not recovered during execution — such a recovery could be introduced in a more advanced VQD variant. The details of each model are discussed in the corresponding device description.

4 Trapped ions

4.1 Trapped ions physical system

The first VQD we discuss is configured to describe a certain type of ion trap system — namely, one in which two ion traps are bridged by a photonic link to generate entangled pairs.

Linking quantum computations across a quantum network is a desirable capability, whether in order to connect remote systems or simply as a means to scale a quantum computer on a single site. The trapped ion qubit system [20] is considered to be one of the most promising options. This is due to its potential for scalability [28, 48], high-fidelity operations [7, 16, 34], and the capability to entangle with photons [52], making it a leading contender for distributed quantum computing.

Practically all multi-qubit ion trap systems are variants on a common paradigm, i.e., a string of ions confined in an oscillating quadrupolar electric field, the Paul trap [74]. There are however many significant variants depending on numerous factors and not least, the specific species of ion (such as calcium, ytterbium, beryllium, magnesium etc). The ion trap VQD that we now describe should be readily adaptable to dif-

ferent classes of ion traps and does not correspond exactly to any specific experimental system described in the literature. Our intent is to capture relevant operational characteristics for a multi-node (i.e. more than one ion trap) system. Gate operations between ions in different traps can be performed by exploiting, at each trap, an ion species suited for remote entanglement (e.g., strontium as in Ref. [94]) and other ions that are well-suited for high fidelity gates and storage (see e.g., [25] for relevant inter-species entanglement transfer). Having configured our VQD we will explore the prospects for entanglement purification, a key enabler for distributed quantum computing. We must of course make specific choices for the available operations, noise models and so on, which we now describe.

The preparation of the state in the trapped ion qubit system is typically achieved via optical pumping. The ions are laser-cooled close to the motional ground state, and then selectively excited and allowed to decay until the population has decayed with a high probability to the target electronic state, which is not coupled to the excitation laser. Readout of the qubits is performed via excitation resonant with state $|1\rangle$ and the detection of the resultant spontaneous photon emission. Dark readout indicates “0” and bright readout indicates “1”. Single and two-qubit gates can be laser or microwave (or RF) driven; the laser-driven method is the reference of our model. We employ the full controlled π -phase rotation (CZ), a native two-qubit gate in this system typically realised via the interaction of a far-detuned bichromatic laser field. This field induces spatially and temporally periodic AC-Stark shifts, producing a qubit-state-dependent force that selectively excites and de-excites the motion of the ions within the trap, imparting a geometric phase conditioned on the collective state of the qubits. This is one of the commonly realised forms of two-qubit gate; other gates such as the Mølmer–Sørensen gate [92] could of course be added to the VQD as a variation.

For the purposes of incorporation into our VQD, we consider remote entanglement as a type of initialisation, where the state of the corresponding ions are erased and set into the Bell state $|\Psi^+\rangle = (|01\rangle + |10\rangle)/\sqrt{2}$ — accompanied by noise defined in the error model. The work described in Ref. [94] is an example; there are many

variants several of which derive from the heralded entanglement scheme by Barrett and Kok[11].

In our trapped ion system, the trap region is divided into two partitions for *storage* and *entanglement* purposes. The storage regions are used for operations that require memory, such as initialisation, readout, operating gates, and physical swaps. On the other hand, the entanglement region is solely dedicated to performing remote entanglement with another trap through a heralded photonic scheme. As a physical example, the traps mentioned in references [10, 38] are segmented or partitioned in a similar manner. Each region is comprised of one or more zones, each physically defined by a number of electrodes and pathways where control signals are delivered to trap and manipulate the ions. The ions can be moved within and between zones through the use of appropriate operations, including *shuttling*, *separation*, *recombination*, and physical SWAP. Shuttling is a linear movement of the ions, separation involves splitting a string of two or more ions into different zones, and recombination is the inverse procedure, necessary before applying a two-qubit gate or swapping the locations of the ions.

Our VQD thus employs a relatively simple shuttling scenario, appropriate to devices that aim at optical linkage for connectivity. More complex shuttling capabilities have been demonstrated through the application of Quantum Charge-Coupled Devices (QCCD), as evidenced by research conducted within both academic and industrial sectors [60, 68, 78]. Penning traps have also recently gained attention as a possible route to 2D shuttling [41]. Systems such as these are interesting targets for VQD simulation in future projects, given the connectivity enabled by such comprehensive shuttling and the corresponding importance of shuttling noise.

4.2 Trapped ions architecture and native operations

We model the trapped ions as a multi-node system, where the user may specify the nodes and the number of ions in each node. For instance, Figure 1 shows a two-node trap we use in our entanglement distillation simulation. The traps are identical and comprise four zones with the same assignments in every segment.

Qubit initialisation to fiducial state $|0\rangle$ can be done to all ions in a single zone at any time, for

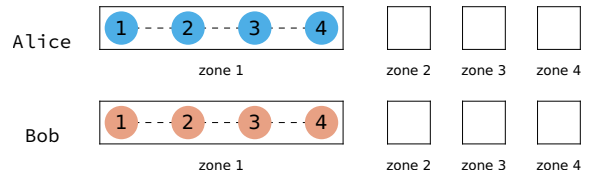


Figure 1: Two-nodes ‘Alice’ and ‘Bob’, each an ion trap, constituting a single VQD system. Alice and Bob each has four ions. This figure shows the arrangement of the ions when instantiated, where all ions lie in zone 1 and are combined. Combined ions are indicated with dashed lines. Qubits initialisation, readout, and physical swaps can be done in zones 1, 2, and 3. Quantum gates (single-qubit rotations and two-qubit controlled phase) are performed in zones 2 and 3. Remote entanglement is performed in zone 4. Linear shuttles are allowed between any neighbouring zones, but separation and recombination cannot be performed in zone 4.

zones 1, 2 and 3. Projective measurement (in the computational basis) can also be done at any time to any ion in zones 1, 2, and 3; however, the ion must be alone in the zone during the readout, as we assume that no individual-ion-resolved fluorescence detection is available. Remote entanglement initialisation to the Bell state $|\Psi^+\rangle$ is done between two parties, and the ions must be in zone 4.

Elementary single-qubit operations include single rotations $\{Rx_j(\theta), Ry_j(\theta), Rz_j(\theta)\}$, where the x - and y - rotations can be performed when the ion j lies in zone 2 or 3. The z -rotations are implemented virtually as in Ref. [63], which are accounted for in the phase of the subsequent gates; thus, z -rotation gates are perfect and instantaneous.

The two-qubit native operations on qubits i and j include the controlled-phase gate $CZ_{i,j}$ and physical swap $SWAP_{i,j}$. To perform these operations, ions i and j must be combined beforehand. However, the implementation of CZ and $SWAP$ gates is different. CZ gates can only be performed in zones 2 and 3, while physical $SWAP$ can be performed in zones 1, 2, and 3.

Ions shuttling is a linear movement, meaning that ions can be moved to another zone as long as there are no other ions in the path. In this mode, combining and splitting moves can be done to ions that are sitting next to each other in a storage zone (zone 1, 2, or 3).

4.3 Error models for our trapped ion VQD

We take it that following state preparation, with a small probability a given ion is outside the level that defines state $|0\rangle$; we consider this the primary noise in the qubit initialisation. The error is modelled with parameterised amplitude damping (Equation (5)) with initialisation fidelity as the parameter. In making this simple choice we are effectively assuming that the probability of initialising to a state outside of the qubit basis is negligible.

As noted earlier, we model the remote entanglement operation as a direct initialisation to the Bell pair $|\Psi^+\rangle \equiv (|01\rangle + |10\rangle)/\sqrt{2}$ for the relevant ions. We model this by initialising the corresponding qubits to state $|\Psi^+\rangle$, followed by noise. Following the indications in Ref. [94], we take the noise to be primarily phase-type (Equation (4)) but with a small component of depolarising noise (Equation (2)). The latter accounts for the non-zero probability associated with even parity states.

The qubit readout error is modelled as symmetric bit-flip noise, with the same errors for both the “0” and “1” outputs. This error model is straightforwardly described by the bit-flip error in Equation (15). To avoid scattering during the optical excitation and classification of outcomes, qubit readout can only be performed on a single ion in a zone.

The noise in the logical single-qubit rotations ($Rx(\theta)$ and $Ry(\theta)$) is modelled as depolarising noise, which captures any unknown interactions during the gate operations. The error severity increases as θ increases, which also corresponds to a longer gate duration.

The dominant source of error in the two-qubit CZ gate is taken to be phase flip noise, which is represented by Equation (4), with a minor contribution from depolarising noise, described by Equation (2). Detailed audits of the noise in laser-driven gates are well-documented in the literature, see e.g., Ref. [94]; the simple choice of noise we make here could be replaced with a form tailored to any given specific system.

In the model, shuttling movements (including physical SWAP) do not result in any specific noise. The noise that occurs during a move is only due to passive noise, which includes an exponential decay of T_1 -relaxation modelled by depolarising noise (Equation (13)) and a Gaussian de-

cay of T_2^* -relaxation modelled by dephasing noise (Equation (12)). The main cost of this operation comes from accelerating and decelerating the ions; this effect is captured in the duration of shuttling. For example, the shuttling duration increases when some ions in zone 1 are moved to zone 3, being $\sqrt{2}$ times longer than when they are moved to zone 2.

4.4 Entanglement distillation on trapped ions

We now describe the use of this VQD to examine an interesting topic: the relative merits of different various entanglement distillations protocols on two remote ion traps. With the help of the virtual device, we can easily identify the best strategy to perform entanglement distillation, and understand how this choice depends on the error assumptions and constraints in the model.

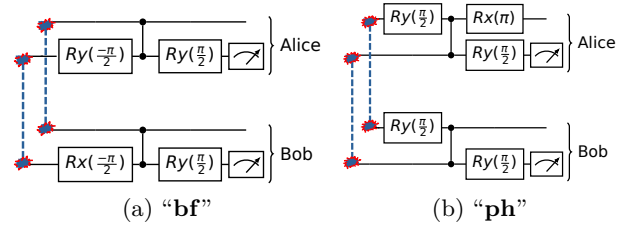


Figure 2: The canonical entanglement distillation circuits – between Alice and Bob – expressed in the native gates of our trapped ion VQD. Circuit (a) mitigates bit-flip error and (b) mitigates phase-flip error. We refer to circuit (a) as “bf” and (b) as “ph”. The blue dashed lines indicate Bell states shared between Alice and Bob. In each circuit presents two pairs of Bell states that have gone through the same distillation steps; the pairs are identical in the ideal case.

In our simulation, we were able to improve the fidelity of a Bell pair from 0.95 to 0.9989. The parameters used in our model are detailed in Table 1. Given such a configuration, the optimal approach would be to perform three rounds of phase-flip correction, as illustrated in Figure 3.

In order to determine the strategy with the highest yield, we simulate up to three rounds of entanglement distillation using our VQD. The simulation is based on the scenario where there are two traps, each containing four ions, as illustrated in Figure 1. In every distillation round, we run the canonical distillation circuits defined in Figure 2.

It is interesting that the best distillation strategy is one that employs exclusively phase-flip cor-

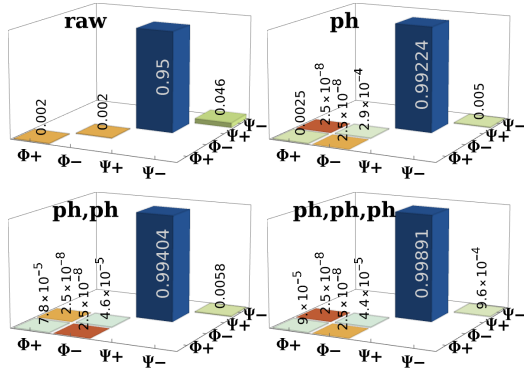


Figure 3: Density matrices tracking the state through an entanglement distillation involving three rounds of phase-flip purification (the best strategy found). The state is shown in Bell basis, where $|\Psi^\pm\rangle = (|01\rangle \pm |10\rangle)/\sqrt{2}$ and $|\Phi^\pm\rangle = (|00\rangle \pm |11\rangle)/\sqrt{2}$. The primary error source in the raw Bell pair is phase flip, with a probability of 0.046 for state $|\Psi^-\rangle$. Hence, the first round of error correction should be phase-flip distillation. After the first round, the phase-flip error is reduced, but it remains the dominant source of error. To further reduce the error, a second and then ultimately a third phase-flip distillation round is applied. Notably, variants where one round is a bit-flip distillation have inferior final fidelity.

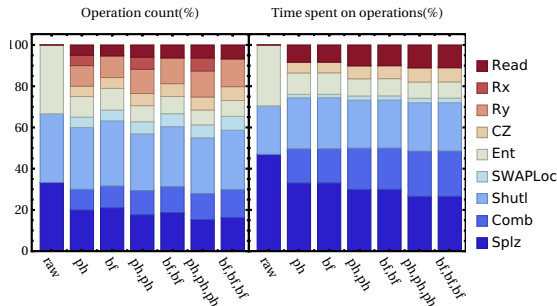


Figure 4: The time profile of the operations involved in the distillation process for a single node, the Alice node. The left figure represents the percentage of the total duration time, while the right figure represents the percentage of the operator count. The overall time required for the process depends on the strategy employed. Acquiring a raw Bell pair takes $0.1ms$, a single round of distillation takes $0.6-0.7ms$, two rounds of distillation take $1.4-1.7ms$, and three rounds of distillation take $3.1-3.8ms$. There are 112 steps involved for three rounds of phase-flip distillation that is listed in Appendix D. Read indicates readout. Quantum gates $Rx(\theta)$, $Ry(\theta)$ and CZ are denoted by Rx, Ry, and CZ, consecutively. The moves such as swap, shuttle, combine, and split are indicated by SWAPLoc, Shut1, Comb, and Splz, respectively.

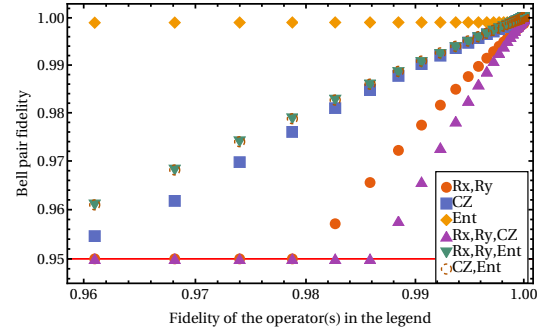


Figure 5: Achievable fidelity for a wide variety of VQD variants and protocols. Each point shows the highest Bell fidelity that can be reached by *any* choice of protocol from: ‘do nothing’, to any combination of ‘bf’ and ‘ph’ over one, two or three rounds (see Fig. 2 for the circuits). Each family of points corresponds to modifying the default fidelity of certain VQD operations – as noted in the key – to the value indicated by the x -axis. The default relevant fidelities are the following: $Fid_{Rx,Ry} = 0.99999$, $Fid_{CZ} = 0.999$, and $Fid_{Ent} = 0.95$. The red line indicates the default fidelity of the raw Bell pair; when points lie on this line, the gate fidelities are so poor that distillation fails to make any improvement.

rection (see Figure 3); this of course stems from the underlying error model. As described earlier, motivated by experimental literature our VQD assigns by far the most severe noise to Bell state generation, and following that, to two-qubit CZ operations. We can confirm from Figure 4 that these components are the primary contributors to the process, and thus the primary sources of noise. Given that dephasing noise is the predominant error present in both operations, it is intuitive that phase-flip correction techniques are the most appropriate.

To gain a deeper understanding of each operator’s role in the distillation process, we modified the fidelity of some operators and selected the Bell pair with the highest fidelity, creating a large number of VQD variants as shown in Figure 5. In each case, we report the best attainable Bell state fidelity. The figure highlights the significance of single-qubit operations: distillation fails entirely when the single-qubit rotations have fidelities below 0.98. Remarkably, one can make some improvement to the Bell pair even with noisy CZ gates; the threshold is around 0.96. Overall, our VQD simulations demonstrate the robustness of standard entanglement distillation circuits, which is an encouraging observation for the prospects of trapped ions distributed QC.

5 NV-centre qubits

We now introduce our second VQD: an NV-centre with its characteristic star topology of two-qubit interactions. We will use this VQD to explore a relatively recent theoretical proposal for exploring a BCS model with a quantum computer.

5.1 NV-centre physical system

The nitrogen-vacancy centre (NV-centre) is a common point defect in diamonds, consisting substitutional nitrogen atom next to a vacant lattice site. The point defect can have a neutral charge (NV^0) or negative charge (NV^-) with triplet spin ($S = 1$). In this quantum system, two kinds of qubits are commonly used for quantum computing purposes: the NV^- electron spin and proximal ^{13}C nuclear spins (abundance of around 1%). Both the electron and nuclear spins are spin-1 systems, two energy levels are deemed to make up a qubit: for example, $m_s = 0$ encodes $|0\rangle$, and $m_s = -1$ encodes $|1\rangle$. The nitrogen (^{14}N) nucleus itself is spin-bearing, and is therefore another potential qubit. If we choose to model this in a given VQD, it is trivial to do so by modifying the gate characteristics of one of the ‘satellite’ qubits accordingly. NV-centre devices of this general kind have been widely studied; for example, researchers at the University of Delft have a considerable body of work including Refs. [3, 12, 22].

The NV-centre is a central-spin system with the electron spin as the centre and it couples the nuclear spins via hyperfine interactions, while the nuclear spins themselves are coupled to each other via weak dipolar interactions [1]. The nuclear-electron coupling strengths are varied depending on the nuclear spin relative position to the electron spin. Such coupling shifts are used to detect, isolate, and coherently control the individual ^{13}C qubit via the central spin. In particular, the hyperfine splittings allow conditional control of the nuclear spins depending on the electron spin state, allowing the realisation of two-qubit gates. Two-qubit gates between nuclear spins are typically realised by a sequence of operations between the nuclear and the electron spins [2, 97]. Single-qubit rotations on the electron spin are realised by microwave pulses, while the nuclear-spin rotations are realised by RF-pulses [2]. However, in such a system, the spins are continuously

coupled with each other; therefore, elective control operations typically consider various echos sequences that isolate unwanted interactions.

5.2 NV-centre architecture and native operations

The NV-centre quantum system has star-shaped connectivity with the electron spin lying in the centre, as shown in Figure 6. Therefore, direct two-qubit operations can only be done between the electron and a nuclear spin.

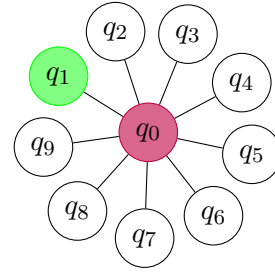


Figure 6: A central spin system (CSS) topology describes the architecture of an NV-centre qubit device. In this example, there are 10 qubits with indices $\{q_0, \dots, q_9\}$. The purple, green, and white nodes correspond to NV^- , ^{14}N , and ^{13}C , respectively. The electron spin always sits in the center with qubit order 0 (q_0). The nuclear ^{14}N spin is numbered as 1 (q_1) — if modelled. Conditional operations can only be done conditioned on the state of qubit q_0 .

Direct initialisation and (destructive) readout of qubits are restricted to the NV^- electron spin. Both processes are done via resonant optical excitation with certain frequencies that are obtained experimentally. Therefore, nuclear spin initialisation and readout — as well as nondemolition measurement — are done via the NV^- electron spin [3]. For instance, the circuits in Figure 7 show initialisation and measurement of a nuclear spin.

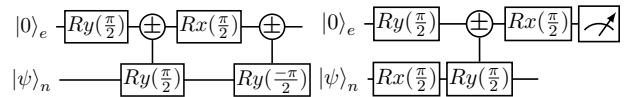


Figure 7: Initialisation via swap (left) and measurement (right) on a nuclear ^{13}C spin. Indices q_0 and q_j indicate NV^- electron spin and ^{13}C nuclear spin, respectively. The electron spin needs to be initialised to state $|0\rangle$, while $|\psi\rangle$ indicates an arbitrary state. The controlled(\pm)- Ry gate, notated as CRy^\pm , is a native NV-center two-qubit operator that is defined in Equation (18).

The native operations of our NV-center virtual device comprise single Pauli rotations on the electron and nuclear spins and conditional Pauli rotations between the electron and any given nuclear spin. The single rotations comprise $\{Rx_q(\theta), Ry_q(\theta), Rz_q(\theta)\}$, where q indicates an electron or a nuclear spin. The $Rz(\theta)$ rotations are implemented virtually in practice [2], which is done by tracking and accumulating the phase that will be incorporated into the phase of the consecutive pulse [63]. The two-qubit gates comprise conditional rotations

$$\{CRx_q^\pm(\theta), CRy_q^\pm(\theta)\}, \quad (17)$$

conditioned to the NV^- electron state, where q denotes a nuclear ^{13}C spin. The NV^- state determines the rotation direction, namely

$$\begin{aligned} CRx_q^\pm(\theta) &:= |0\rangle\langle 0|_{q_0} \otimes Rx_q(\theta) + |1\rangle\langle 1|_{q_0} \otimes Rx_q(-\theta) \\ CRy_q^\pm(\theta) &:= |0\rangle\langle 0|_{q_0} \otimes Ry_q(\theta) + |1\rangle\langle 1|_{q_0} \otimes Ry_q(-\theta) \end{aligned} \quad (18)$$

where q is an index of a ^{13}C spin.

5.3 Error models for our NV-centre VQD

A high-fidelity electron spin initialisation comprises two stages: optical pumping to obtain NV^- from NV^0 , and initialisation of NV^- to spin $m_s = 0$ (state $|0\rangle$) that is indicated with photon emissions [85]. We model this by amplitude damping (Equation (5)), in which the parameter directly denotes initialisation infidelity.

The NV^- electron qubit readout is modelled with a projective measurement in the computational basis $M_0 = \{|0\rangle\langle 0|, |1\rangle\langle 1|\}$. Recall that, qubit readout is performed by applying the readout frequency that is resonant with $m_s = 0$ excitation: detecting a photon means state $|0\rangle$ (or a dark count error) while seeing no photon means state $|1\rangle$ (or a loss error). Our model considers only errors caused by photon loss, as the probability of dark count is typically very low. Hence, the readout error is asymmetric: given an input state $|1\rangle$ measurement is correctly “1”, but input $|0\rangle$ can lead to either “0” or “1”.

For this, we model the measurement error with an inverted amplitude damping (Equation (5)), which “decays” the qubit toward state $|1\rangle$,

$$q_0 \text{---} [X] \text{---} [damp(p)] \text{---} [X] \text{---} \begin{array}{c} 0/1 \\ \diagup \diagdown \end{array} \text{---} [damp(1)] \text{---}, \quad (19)$$

where p is measurement bias; this gives an appropriate rate of incorrect “1” results on input $|0\rangle$. The final damping fully resets the qubit to $|0\rangle$; this represents the ultimate effect of the repeated measurement process which effectively drives the state to $|0\rangle$. Therefore, the p used here should be the net (rather than per-measurement) probability that an actual $|0\rangle$, pre-measurement, is recorded as a ‘1’.

It is important to mention that our measurement model oversimplifies some of the processes occurring in the experiment. Specifically, incorrect assignment of the measurement outcome has the potential to completely dephase the nuclear spins, given that their evolution frequencies depend on the NV electron state. Additionally, the dark count, while potentially very low ($<0.1\%$), is still an important consideration in the context of repeated measurements, as is typical in actual practice. Despite these complexities, we proceed under the assumption that the fidelity of our measurement model adequately reflects the statistical distribution of such outcomes. Consequently, the assumed measurement fidelity in this model is based on the premise of repeated measurements having been performed.

The physical quantum gates experience standard dephasing and depolarising forms of noise, while the virtual gate $Rz(\theta)$ can only experience dephasing noise. In practice, the virtual gates are often modelled to be perfect. Noisy single gate rotations $Rx(\theta)$ and $Ry(\theta)$ are followed by single-qubit depolarising (Equation (1)) and dephasing (Equation (3)) noise. Noisy two-qubit gates CRx^\pm and CRy^\pm are followed by two-qubit depolarising (Equation (2)) and dephasing (Equation (4)) noise. The proportion of depolarising and dephasing noise are adjustable as per the method discussed in Section 3.2.

Noise acting on the passive qubits involves free induction decay corresponding to T_1 (Equation (13)) and T_2 (Equation (11)), and cross-talk in the form of ZZ -coupling between all possible pairs of nuclear ^{13}C qubits. Our VQD by default incorporates the assumption that dynamical decoupling is constantly implemented on the passive qubits; this is supported by the common experiment practice in order to achieve long-coherence qubits [4, 15] and to perform decoherence-protected gates [2, 107]. Therefore, we use the T_2 as the phase decay rate, and

gate implementation is done serially. The ZZ -coupling captures the slow (a few Hertz) but constant unwanted entangling dipolar interaction among the nuclear qubits.

5.4 BCS model simulation on NV-centre

As noted in the previous sections, the NV centre has a characteristic topology wherein multiple nuclear spin qubits can interact with a common core, but not with each other directly. A recent paper, “Digital quantum simulation of the BCS model with a central-spin-like quantum processor” [86] explores the utility of exactly such a topology for the dynamics Bardeen–Cooper–Schrieffer (BCS) models – the authors note that NV centres are a natural match to their required geometry. This affords an intriguing opportunity to test our NV Centre VQD – through the use of the VQD we can determine how experimentally challenging it would be to perform an accurate simulation on a modest scale.

To maximise the prospects for the approach, we opt to synthesise compact circuits that are propagators of the BCS Hamiltonian; for this we use a recently discussed *subspace compilation* method [33, 64]. Then, we translate the resulting circuit into the native operations of our NV-centres. Finally, we examine the simulation performance under various scales of noise.

We follow the prescription of Ruh et al.[86], who explain that a relevant BCS model can be connected to central spin systems with the Hamiltonian,

$$H_{\text{BCS}}(t) = -g(t) \sum_{q=0}^{n-1} \epsilon_q H_q(t) + g(t) L^z + g(t) (L^z)^2, \quad (20)$$

where ϵ_q is energy orbital, $g(t)$ is the magnetic field quench. In the context of interest for Ruh et al., the Gaudin Hamiltonians H_q can be defined as

$$H_q(t) = \sum_{j=0, j \neq q}^{n-1} \frac{\boldsymbol{\sigma}_q \cdot \boldsymbol{\sigma}_j}{2(\epsilon_q - \epsilon_j)} + \frac{\sigma_q^z}{g(t)}, \quad (21)$$

where $\boldsymbol{\sigma} \equiv (\sigma^x, \sigma^y, \sigma^z)$ is a Pauli vector.

Ruh et al. note that the model is integrable when parameters are suitable constants, but that by considering a time-varying $g(t)$ one can realise a quench. They consider the scenario where g

switches (smoothly, via a compact S-curve) from a base value to an increased value, before then switching back to base. We follow their implementation, see Figure 8. The authors monitor the quantity called the return probability which they denote $\mathcal{R}_{\text{exact}}$ and we write as follows

$$\text{Fid}(\psi_t, \psi_0) = |\langle \psi_0 | \mathcal{T} [e^{-\frac{i}{\hbar} \int_{t'=0}^{t'=t} H_{\text{BCS}}(t') dt'}] | \psi_0 \rangle|^2, \quad (22)$$

as it is the state’s fidelity with respect to the initial state at $t = 0$ (ψ_0). Here \mathcal{T} is the time-ordering operator. The initial state $|\psi_0\rangle$ is the ground state of the H_{BCS} at $t = 0$ that is obtained exactly. With this setup, we can observe the oscillation around the quench as shown in the second figure of Figure 8. The simulation is done for $n = 5$ qubits and the orbital energy levels are defined as simple non-interacting harmonic oscillators as per reference [86].

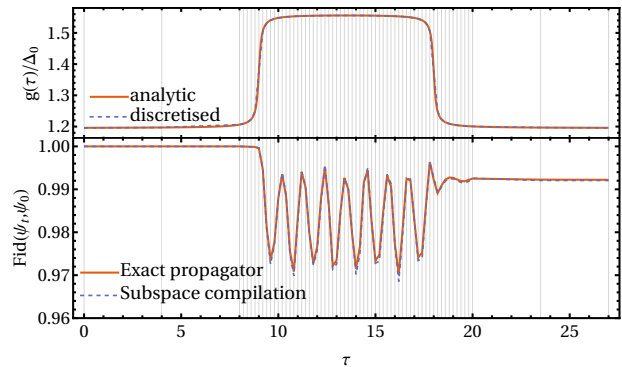


Figure 8: A quench is driven by varying g within H_{BCS} as shown in upper panel. The corresponding ‘return probability’ $\text{Fid}(\psi_t, \psi_0)$ defined in Equation (22) is shown in the lower panel. The horizontal axis (τ) is scaled time to the unit energy as per Ref. [86]. The grey lines indicate time discretisation comprising 64 partitions; thus involving 64 propagators. We use the exact initial state of H_{BCS} at $t = 0$. The propagators are computed exactly using Mathematica function `MatrixExp`, and approximated with circuits obtained via the subspace compilation method introduced in [33, 64].

To simulate dynamics of a BCS model, as the authors of [86] note the state at t is evolved with respect to that at t_0 by an operator,

$$U(t, t_0) = U(t = t_m, t_{m-1}) \dots U(t_1, t_0)$$

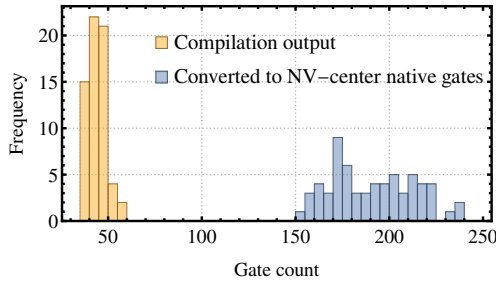
with

$$U(t_j, t_{j-1}) \approx e^{-i/\hbar H(t_{j-1})(t_j - t_{j-1})}$$

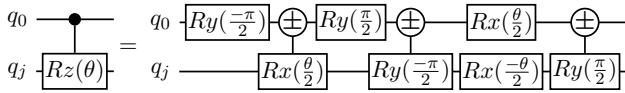
provided that $t_j - t_{j-1}$ is sufficiently small. Each $U(t_j, t_{j-1})$ must then be expressed as an NV-

compatible circuit. A canonical solution is Trotterisation as employed in [86] to express the Gaudin terms, the most complex terms in H_{BCS} . Even though the Gaudin term employs only one SWAP gate to have star-shaped connectivity, the gate count in Trotterisation increases severely with the desired accuracy; we find this can require around one thousand gates for each propagator $e^{-i\Delta t H_{\text{BCS}}(t)}$ to obtain fidelity accuracy at least 10^{-3} . Consequently, if hardware noise were present at any meaningful level, the output would be almost totally corrupt.

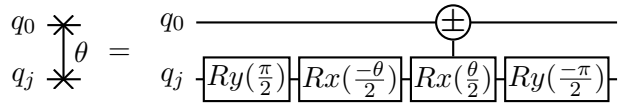
As an alternative, we can use *ab initio circuit synthesis* methods to find circuit realisations. Moreover, the present case is especially suitable as it allows us to take advantage of the block-diagonal form of H_{BCS} — we can employ a recent subspace compilation method introduced in [33, 64]. Here, an adaptive variational procedure synthesises a circuit to closely mimic a defined target; the ‘subspace’ qualifier means that



(a) Propagators gate counts



(b) Controlled-z rotation expressed in native NV-center gates



(c) Parameterised swap expressed in native NV-center gates

Figure 9: The resulting gate count of subspace compilation of H_{BCS} propagators before and after conversion to the native NV-centre gates are shown in (a). The gate pool has a star topology with electron spin q_0 as the central spin: $\{Rz_{q_k}(\theta), C_{q_0}Rz_{q_j}(\theta), SWAP_{q_0,q_j}^\theta\}$, where $k \in \{0, \dots, n-1\}$ and $j \in \{1, \dots, n-1\}$. The controlled-z rotations $C_{q_0}Rz_{q_j}(\theta)$ are converted to the native NV-centre gates by circuit (b). The parameterised swaps are expressed in the native NV-centre gates by circuit (c). The controlled(\pm)-rotations are defined in Equation (18).

the target need only be matched *within* a defined subspace of interest and is free to diverge arbitrarily elsewhere. We can safely permit this freedom since, by construction, H_{BCS} is spin-preserving and thus block diagonal, because it only rearranges the energy levels that are occupied by the Cooper pairs [86]. We compile each H_{BCS} propagator in the subspace that preserves the spin of the initial state (that of Hamming weight one).

This initial compilation is not to the NV-native gates, but rather to a gate set that naturally corresponds to the Hamiltonian structure. As one might hope, this produces very compact propagators with gate counts 35-70, as shown in Figure 9. Specifically, we set the gate pool with a star topology:

$$\{Rz_{q_k}(\theta), C_{q_0}Rz_{q_j}(\theta), SWAP_{q_0,q_j}^\theta\},$$

where $k \in \{0, \dots, n-1\}$ and $j \in \{1, \dots, n-1\}$ and q_0 is set to be the electron NV⁻ spin. Gate $C_{q_0}Rz_{q_j}(\theta)$ is controlled-z rotation with the controlled qubit is the electron spin q_0 . Gate $SWAP^\theta = \exp(-i\frac{\theta}{2}(XX + YY + ZZ))$ is parameterised swap gate, where the full swap is achieved when $\theta = m\pi$ for any integer m . Those gates are chosen for their Hamming weight-preserving property. The resulting circuits are then converted into the native NV-centre gates as shown in Figure 9. They then typically include about 200 gates, still vastly more compact than the direct Trotter approach (and moreover, propagators $U(t_m, t_{m-1})$ can correspond to substantial time periods $t_m - t_{m-1}$ when the function $g(\tau)$ is not changing appreciably).

Having thus expressed the complete sequence of propagators using the native NV-centre gates, we now can estimate the dynamics of H_{BCS} on our NV-centre VQD. First, we perfectly prepare the initial state as the exact H_{BCS} ground state for $t = 0$. We apply the noisy form of the propagators and calculate the return probability (Equation (22)) on each time step. Note that, as we assume a continual dynamical decoupling sequence is applied to the passive qubits, our circuits are implemented in serial manner; this has the implication that they suffer more noise. We measure the performance on various scales of gate noise, with the results shown in Figure 10.

Figure 10 shows a poor simulation performance on the realistic noise setting, even for the first propagator. That is expected since the first propagator comprises 202 gates – much larger than

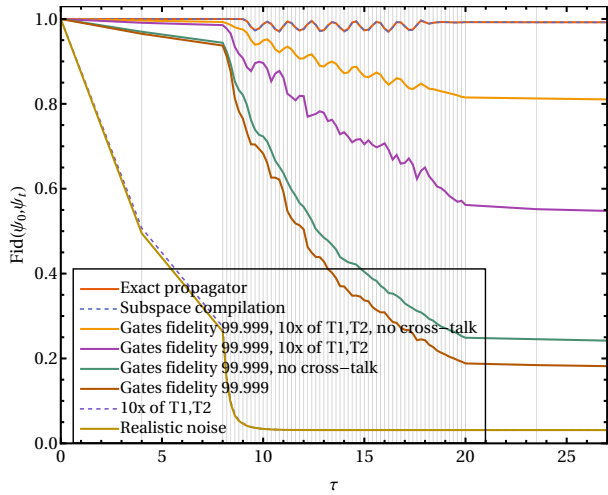


Figure 10: Simulation of H_{BCS} dynamics for various serveries of NV-centre noise. There are 64 propagators with the scaled time unit (τ) as per Ref. [86]. The initial state is set to be perfect and exact at $t = 0$. The realistic noise configuration is given in Table 2 in the Appendix. Various scale of noise is tried out as shown in the figure; the value on the realistic noise setting is used when not mentioned. See Figure 8 as a reference to the quench function $g(\tau)$.

the state-of-the-art complex experiment [2]. Interestingly, the oscillation is already observed by setting the gates' fidelities to 0.99999 (see the maroon line in Figure). Moreover, a clear quasi-periodic oscillation manifests when more aspects are improved, i.e., high gate fidelities, longer coherence time and the absence of crosstalk (see the orange line).

The sobering conclusion is that even the ultra-weak nuclear-nuclear crosstalk, if left unmitigated, is sufficient to significantly degrade the model. We would anticipate that increasing the number of qubits to increase the complexity of the isomorphic BCS model, would correspondingly amplify these issues. However, we have not explored error mitigation strategies such as zero-noise extrapolation or quasi-probability constructions [55, 98], let alone the more recent methods [17], and these might alleviate the fidelity requirements very significantly – an interesting topic for future study, and (needless to say) very straightforward to investigate with the VQD tool.

6 Neutral atoms

6.1 Neutral atoms physical system

Our neutral atom VQD is based on experimental hardware platforms that exploit quantum registers composed of arrays of individually trapped neutral atoms [67]. Each atom encodes a single qubit for alkali atoms such as Rb or Cs by using hyperfine ground-state transitions with microwave frequency separations, whilst for alkaline earth systems using Sr and Yb qubits can be encoded optically via narrow clock transitions using the long-lived intermediate triplet states. Qubit initialisation, state preparation, quantum gates and readout are all performed using lasers providing access to both global and single-site operations. Measurements are performed using fluorescence detection.

A major advantage of the neutral atom platform is scalability, with the ability to prepare various geometric configurations in 1D, 2D and 3D with up to 1000 qubits [8, 9, 39]. This can be combined with moving optical tweezers to permit dynamic reconfiguration of the qubit register during computation [14], providing flexible connectivity.

To engineer coupling between atomic qubits, atoms are excited to Rydberg states, offering strong long-range dipole-dipole interactions. These interactions result in a blockade effect at short range [57] whereby only a single atom can be excited to the Rydberg state within a radius of 5-10 μm . This blockade mechanism can be exploited to implement two- or multi-qubit gates such as Toffoli gates with arbitrary numbers of control qubits [40, 47, 54]. Recent experimental demonstrations have shown these gates can be implemented with high fidelity in systems with 60 qubits [27] in parallel, making neutral atoms a promising candidate for scalable quantum computing.

6.2 Neutral atoms architecture and native operations

The architecture of the virtual neutral atoms is entirely configurable by the end-user, who specifies the initial geometry (a list of positions for each atom), blockade radius, and probability of atom loss during reconfiguration. The geometry is arbitrary and can involve a 3D configuration,

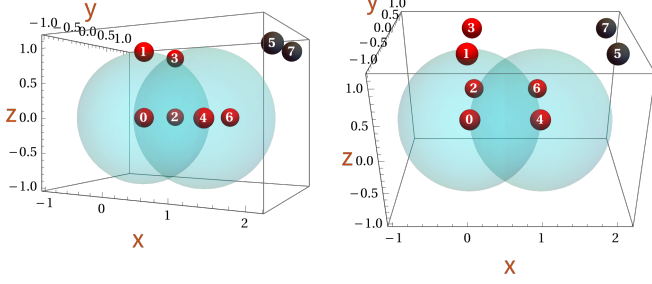


Figure 11: A 3D lattice configuration of a virtual Rydberg neutral atoms. The red dots indicate the atoms and their corresponding qubit indices. The user can display the blockade radii of selected atoms, as shown for atoms 0 and 4. To perform multi-qubit operations, the atoms must be within the overlapping blockade radii, e.g., as in the case of atoms 0 and 4 in the picture, enabling a two-qubit gate between them. The user can also choose to display the last position of missing atoms, represented by grey atoms. In this example, atoms 5 and 7 are lost to the environment.

with visual aids available to assist the user. For instance, Figure 11 shows a 3D configuration that visualizes two overlapping blockade radii and two atoms that are lost to the environment, which is an additional error mechanism compared to other qubit platforms.

In our virtual neural atoms, it is possible to initialise or reset qubits at any time, either individually or acting on the whole register simultaneously, reflecting the process of trapping and optical pumping of atomic qubits into $|0\rangle$.

The qubit readout can be performed concurrently, where it is modelled by performing projective measurement in the computational basis. The measurement process is based on the method used in reference [71], where in practice, it may also induce atom loss to the environment.

Reconfiguring the register is accomplished by utilising two fundamental move operations: location shift ($ShiftLoc_{\mathcal{Q}}(\mathbf{v})$) and location swap ($SWAPLoc_{p,q}$). The $Shiftloc_{\mathcal{Q}}(\mathbf{v})$ operator shifts the position of atoms in set \mathcal{Q} by a vector \mathbf{v} , while the $SWAPLoc_{p,q}$ operator exchanges the positions of atoms p and q .

An arbitrary single qubit unitary is achieved by optical control [102, 106], by driving two-photon Raman transitions far detuned from an intermediate excited state facilitating rapid population transfer between states $|0\rangle$ and $|1\rangle$. By configuring the phase (ϕ), two-photon detuning (Δ),

and duration of the laser (t), an arbitrary single unitary can be achieved as follows

$$U(\phi, \Delta, t) = \begin{pmatrix} \cos(\frac{\tilde{\Omega}t}{2}) - i\frac{\Delta}{\tilde{\Omega}} \sin(\frac{\tilde{\Omega}t}{2}) & -i\frac{\Omega}{\tilde{\Omega}} \sin(\frac{\tilde{\Omega}t}{2})e^{i\phi} \\ -i\frac{\Omega}{\tilde{\Omega}} \sin(\frac{\tilde{\Omega}t}{2})e^{-i\phi} & \cos(\frac{\tilde{\Omega}t}{2}) + i\frac{\Delta}{\tilde{\Omega}} \sin(\frac{\tilde{\Omega}t}{2}) \end{pmatrix}, \quad (23)$$

where $\tilde{\Omega} = \sqrt{\Omega^2 + \Delta^2}$, and Ω indicates the Rabi frequency. For instance, a Hadamard gate can be obtained by operator $U(\phi = 0, \Delta = \Omega, t = \pi/\tilde{\Omega})$ and a rotation $Rx(\theta)$ can be achieved by operator $U(\phi = 0, \Delta = 0, t = \theta/\Omega)$.

When two or more Rydberg atoms are excited within a certain distance of each other, they experience a strong interaction that prevents any further excitations within this distance, known as the blockade radius. The interaction leads to the accumulation of a phase that depends on the state of the other atoms within the blockade radius. This phase accumulation is the basis for many multi-qubit gate implementations and determines parallel execution of quantum gates. This process is also known as Rydberg blockade mechanism [5, 100].

We approximate the Rydberg interaction as a hard 2- or 3-dimensional sphere with radius R_b , defining the interaction zone r_{int} (refer to Figure 12). Consequently, when two or more atoms are within their respective interaction zones, they can interact and execute multi-qubit gates. These interacting atoms collectively form what is termed a *restriction zone*, a union of their interaction zones. This restriction zone inherently limits the parallel execution of other quantum gates within. Figure 12 illustrates these zones, and for more detailed information, see reference [88]. Our tool accommodates such a Rydberg blockade mechanism and provides automatic parallelism of quantum operations that adhere to these restriction zones. Appendix E provides an explicit example of such parallelism.

Based on many proposed and available techniques [13, 13, 54, 76, 80, 99], we provide the following operations as the native multi-qubit gates

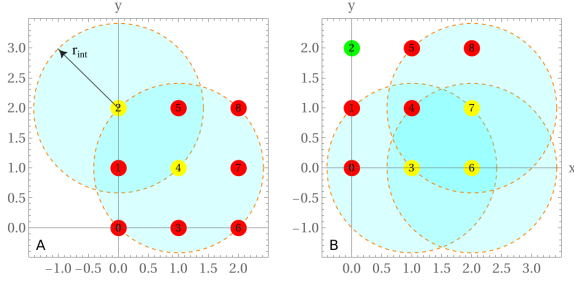


Figure 12: In panel A, the interaction zones of the yellow atoms (2 and 4), each with radius r_{int} , are depicted with the blue area. Since they are within each other's interaction zones, atoms 2 and 4 can execute a two-qubit gate. In panel B, the yellow atoms (3, 4, and 7) are actively interacting, i.e., performing a three-qubit gate, thus, the resulting restriction zone encompasses the entire blue area. Consequently, only a gate acting upon atom 2 can be executed in parallel with this three-qubit gate.

in our neutral atom VQD.

$$CZ(\phi)_{p,q} = \begin{pmatrix} 1 & 0 & 0 & 0 \\ 0 & e^{i\phi} & 0 & 0 \\ 0 & 0 & e^{i\phi} & 0 \\ 0 & 0 & 0 & e^{i(2\phi-\pi)} \end{pmatrix} \quad (24)$$

$$C_{\mathcal{Q}}Z_p = i(|2^k-1\rangle\langle 2^k-1|_{\mathcal{Q}}Z_p + \sum_{j=0}^{2^k-2} |j\rangle\langle j|_{\mathcal{Q}}I_p) \quad (25)$$

$$C_pZ_{\mathcal{Q}} = i \prod_{j \in \mathcal{Q}} (|0\rangle\langle 0|_p I_j + |1\rangle\langle 1|_p Z_j), \quad (26)$$

where p and q indicate single atom indices, and \mathcal{Q} denotes a set of atom indices with cardinality k . Parameter ϕ is a phase provided by the user that captures the accumulated phase in the process. To implement the $CZ(\phi)_{p,q}$ gate, the blockade radii of atoms p and q must overlap in which atoms p, q must lie within. The multi-qubit operators $C_pZ_{\mathcal{Q}}$ acts as the one-control (atom p) of the multi- Z operator applied to atoms in \mathcal{Q} , while the $C_{\mathcal{Q}}Z_p$ acts as the multi-control (all atoms in \mathcal{Q}) of the Z operator applied to atom p . To simplify the phase-dependence associated with the blockade mechanism, every atom in $\{p\} \cup \mathcal{Q}$ must be within their overlapping blockade radii, as illustrated in Figure 12. In our VQD, the blockade condition must be met whenever any of these gates are applied, in order to reflect the blockade mechanism. The question of whether two qubits can interact is therefore a binary one: they can if they are within the radius, otherwise they cannot. Of course, a further extension of this VQD could

impose a more nuanced rule whereby phase acquisition rate, and indeed error rates, vary continuously with separation. In any case, the end-user's code must take into account any reconfiguration of the register between gate applications.

6.3 Error models for our neutral atoms VQD

Device initialisation involves loading a cold ensemble of neutral atoms into the desired register configuration using optical tweezers [8, 9, 26]. Each atom encodes a single qubit; the computational basis corresponds to ground-state hyperfine levels and is initialised through Raman cooling. Imperfect cooling results in some population leakage outside of the computational basis; we can describe this leakage as a completely positive and trace-nonincreasing (CPTN) map. Noisy qubit initialisation is described as a perfect damping (Equation (5) with $p = 1$) that resets the qubit to $|0\rangle$, followed by a CPTN map consisting of operator

$$L = \begin{pmatrix} \sqrt{1-\gamma} & 0 \\ 0 & 1 \end{pmatrix}, \quad (27)$$

where $0 \leq \gamma \leq 1$ denotes the probability of leakage during initialisation. Notice that $L^\dagger L \leq I$ and is completely positive, and thus it fulfils the requirements of the CPTN map. In practice, the effect is to attenuate the total probability associated with system's state, with the 'missing' probability associated with leakage events that are not tracked further within the model.

Readout is achieved by pumping atoms from state $|1\rangle$ into a stretched state that enables their distinction from those in state $|0\rangle$ [53]; then a fluorescence image can be taken to determine the occupancy of the array sites. This method is often accompanied by atom loss ($\leq 2\%$), which increases with the number of measurements. We model this noisy measurement as depolarising noise (Equation (1)) accompanied with a list that tracks accumulated atom loss probability due to measurement. After a measurement, a pseudo-random number is generated to determine if the atom is still present or lost to the environment.

The error in implementing a single-qubit unitary $U(\phi, \Delta, t)$ in Equation (23) mainly comes from the characterisation of noise in Raman transition, which is dominated by phase-type errors (Equation (1)) with the error parameter $\alpha =$

$(1 - e^{t/2T_2})$ and a small fraction of bit-flip error. The parameter α corresponds to the probability of a phase flip occurring during the gate duration t . There is a finite bit-flip error probability which is typically asymmetric, i.e., probability of the event $|0\rangle \mapsto |1\rangle$ is not equal to the event $|1\rangle \mapsto |0\rangle$.

The realization of the two-qubit $CZ(\phi)$ gate utilises the blockade mechanism in highly excited Rydberg states. The typical error in this mechanism arises from spontaneous emission from Rydberg states, associated with the possibility of the system decaying to states outside the computational basis. We model this error using a CPTN map consisting of the following single operator:

$$K = \begin{pmatrix} 1 & 0 & 0 & 0 \\ 0 & \sqrt{1-\alpha} & 0 & 0 \\ 0 & 0 & \sqrt{1-\alpha} & 0 \\ 0 & 0 & 0 & \sqrt{1-\beta} \end{pmatrix}, \quad (28)$$

where α and β correspond to the probability of decay to a state outside the computational basis during the excitation time. Typically, α and β have different values, as they correspond to distinct paths in the process. Notice that $K^\dagger K \leq 1$ and the map is completely positive.

For multi-qubit gates, we implement a similar noise model as for the two-qubit gates. Let \mathcal{Q} be the set of qubits involved in multi-qubit gate operations, the error during the process is described with a CPTN map that comprises the following single operator

$$M = \bigotimes_{j \in \mathcal{Q}} M_j \quad M_j = \begin{pmatrix} 1 & 0 \\ 0 & \sqrt{1-\alpha} \end{pmatrix}, \quad (29)$$

where α is the leakage probability.

The passive qubits undergo free induction decay, characterised by T_1 and T_2 times. The T_1 time is fundamentally limited by the vacuum lifetime of each atom, denoted as T_{vac} . This can be approximated using the relationship $T_1 = T_{vac}/N$, where N signifies the number of atoms present in the vacuum chamber. This estimation characterises the *collisional loss* rate, which corresponds to the rate of collision with untrapped background atoms; hence, this rate serves as the upper bound for T_1 [87]. The T_1 decay is modelled using depolarising noise (Equation (13)), while the T_2 decay is modelled with dephasing noise (Equation (11)). Both types of noise account for energy loss and information loss resulting from collisions with background atoms.

Reconfiguring the atoms (a ‘move’) is accomplished through the manipulation of optical tweezers. The move operators constitute operations that modify the atoms’ locations such as *SWAPLoc* and *ShiftLoc*. The process typically requires a substantial duration in practice, on the order of hundreds of microseconds. Additionally, atoms in motion acquire extra heat – especially when they are moving fast, resulting in an enhanced dephasing process. The errors acquired during this process constitute the depolarising T_1 decay (Equation (13)) and the enhanced dephasing κT_2 -decay to account for the thermal effect, namely,

$$deph \left(\frac{1 - e^{-\kappa \Delta t / T_2}}{2} \right), \quad (30)$$

where the factor $\kappa \geq 1$ intensifies the decay due to the presence of heat. Ideally, κ is affected by the speed and the distance of the moves; for simplicity, we set κ to be a constant.

6.4 Graph state construction and Steane code preparation on Neutral Atoms

Here, we replicate a recent neutral atom experiment presented in [14] in our virtual neutral atom device. The experiment involves the preparation of a 1D linear cluster state and a seven-qubit Steane code logical state, followed by stabiliser measurements to benchmark the resulting states. Both of these states are graph states [35], which can be efficiently represented using graphs as illustrated in Figure 13. In these graphs, vertices correspond to plus states $|+\rangle := (|0\rangle + |1\rangle)/\sqrt{2}$, and edges represent controlled- Z gates. The preparation of such states requires the generation of multiple non-local connections, which can be carried out concurrently on a neutral atom platform.

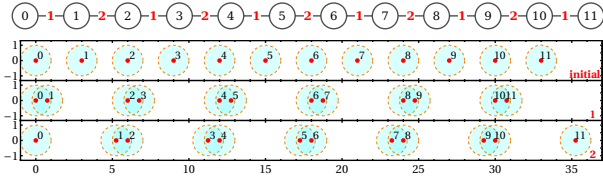
Given a graph $G = (V, E)$ that comprises a list of vertices V and edges E , the corresponding graph state $|\Psi_G\rangle$ can be written as

$$|\Psi_G\rangle = \prod_{\{i,j\} \in E} CZ_{i,j} \bigotimes_{v \in V} |+\rangle_v \quad (31)$$

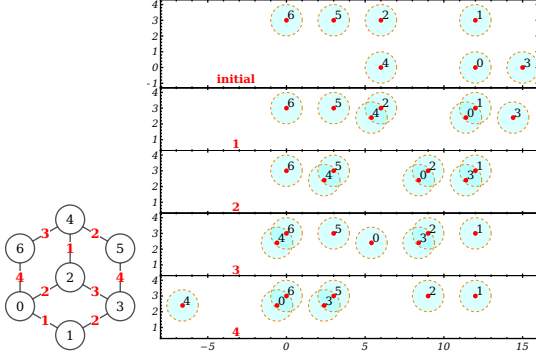
that is stabilised by a set of stabilisers

$$\mathcal{S}_G = \{X_j \bigotimes_{k \in N_G(j)} Z_k \mid j \in V\}, \quad (32)$$

where $N_G(j)$ is neighborhood of atom j . In the following, we emulate the preparation of two



(a) 1D cluster state.



(b) Seven-qubit Steane code logical state.

Figure 13: Representation and preparation of a 12-qubit 1D cluster state and seven-qubit Steane code logical state. The graph representation of each graph state is shown using white circles and numbered edges; the quantum register configurations involved in the process are depicted in the tables. Numbered red dots represent atoms, blue disks indicate the blockade radii of the atoms, and numbered edges correspond to the atom configurations required to implement the entangling gates that operate concurrently. The initial register configuration is labelled “initial,” followed by a sequence of configurations implementing controlled- Z gates. Having the atoms within the overlapping blockade radii, denoted by overlapping blue disks, is necessary to implement two-qubit gates between them.

graph states and measure their stabilisers given graphs shown in Figure 13.

The preparation of a 12-qubit linear 1D cluster state is achieved using the three sequential atomic configurations illustrated in Figure 13a. We measure the expected values of each stabiliser S_j , where S_j is defined by Equation (32) with the graph given in Figure 13a. The resulting expected values in Figure 14a are obtained from 2000 simulated measurements. Error parameters are manually adjusted to fit the experimental results. The average of stabiliser measurements in the simulation is $\langle S_i \rangle = 0.87$, which is equal to that in the experiment. Without the SPAM errors, we obtain $\langle S_i \rangle = 0.97$, while the experiment yields $\langle S_i \rangle = 0.91$.

Preparing a logical seven-qubit Steane code can be achieved using five register configurations, as

illustrated in Figure 13b. Here, the logical state $|+\rangle_L \equiv (|0\rangle_L + |1\rangle_L)/\sqrt{2}$ is prepared by applying the transversal Hadamard gate to the logical state $|0\rangle_L$, i.e., applying a Hadamard gate to each qubit. The expected value of each stabiliser and logical Pauli operators X_L and Z_L are measured. The stabiliser is defined by Equation (32) with the graph given in Figure 13b. The logical Pauli operators are defined as $X_L = X_0X_1X_3$ and $Z_L = Z_0Z_1Z_3$, which ideally result in $\langle X_L \rangle = 1$ and $\langle Z_L \rangle = 0$ for the logical state $|+\rangle_L$. The measurement results are shown in Figure 14b, obtained by simulating 2000 measurements. The average expected values of the plaquette X and Z operators are $\langle S_X \rangle = 0.51$ and $\langle S_Z \rangle = 0.73$, respectively, which the numbers agree with the experiment. The expected value of the logical Pauli measurements in the simulation are $\langle X_L \rangle = 0.76$ and $\langle Z_L \rangle = -0.02$, while the experiments yield $\langle X_L \rangle = 0.71$ and $\langle Z_L \rangle = -0.02$.

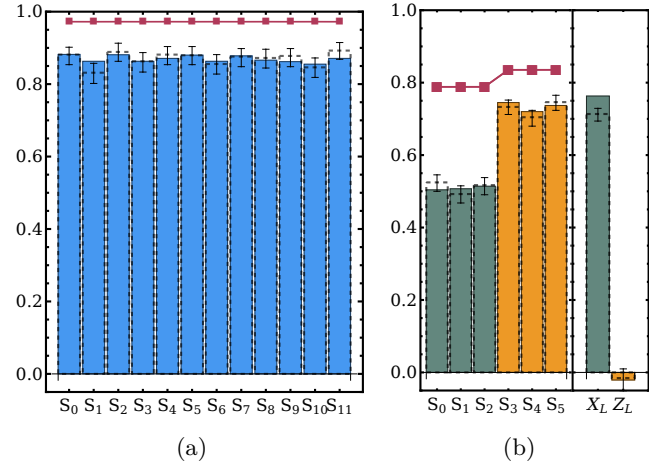


Figure 14: Measurement statistics of: (a) stabilisers of the 1D cluster state with the graph shown in Figure 13a, and (b) stabilisers (left) and logical X and Z measurements (right) of the seven-qubit Steane code prepared in the logical state $|+\rangle$, with the graph shown in Figure 13b. The green and orange bars indicate plaquette operators of X (S_0, S_1 , and S_3) and Z (S_3, S_4 , and S_5), respectively. We took 2000 shots of simulated measurements for each operator. The square markers indicate the results without SPAM errors. The dashed bars denote the results from the experiments performed in [14]. The error parameters used in this simulation are tabulated in Table 3 in the Appendix.

It is important to emphasise that simplifications have been implemented for practical purposes. For example, as noted earlier we model the blockade as a hard-edged sphere, neglecting

the finite range of dipole-dipole interaction – in the magnitude of R^{-6} – that may impact the outcomes. Consequently, some discrepancies in the distribution profile and expected values compared to experimental results are to be anticipated. However, in certain cases, we have managed to achieve values that precisely match those obtained in the experiments.

7 Silicon qubits

7.1 Silicon qubits physical system

Electron spin qubits in semiconductor quantum dots [56, 101] utilise the inherent two-level property of the spin- $\frac{1}{2}$ of electrons to encode states $|0\rangle$ and $|1\rangle$. This is achieved by confining individual electrons in an electrostatic potential well – a quantum dot – that can be controlled with voltages while subjecting them to a magnetic field. A typical platform is composed of an array of quantum dots with one or three electrons in each well [77]. The dots containing three electrons are typically utilised as a part of the spin-to-charge readout method, i.e., spin parity readout [89]. The tunnelling barriers between quantum dots can be adjusted via dedicated gate voltages to engineer electrically controlled two-qubit exchange interactions. Furthermore, the fabrication of the platform is compatible with advanced semiconductor manufacturing techniques in some cases. The same lithographic process that is used in commercial foundries to create silicon chips for devices such as laptops or smartphones, can be employed to create quantum-dot array devices. Therefore, spin qubits possess the potential as a scalable quantum computing platform due to their practicality in control, well-known fabrication techniques, long coherence time, and the tiny size that may enable integration of many millions of qubits in a single chip.

There are several semiconducting materials proposed to implement a spin qubit quantum processor, such as GaAs and germanium. However, here, we focus on silicon as the material to host the spin qubits with the quantum dots being defined in the ^{28}Si quantum well of the $^{28}\text{Si}/\text{SiGe}$ heterostructure. In particular, our silicon VQD platform is configured to correspond to a recent device at the University of Delft [77]; our error model is configured by analysing the description and characterisation of the device reported by the

authors of that paper.

7.2 Architecture and native operations on virtual silicon qubits

Our silicon virtual quantum device has a 1D linear architecture, with nearest-neighbour interactions. For simplicity, we take it that each quantum dot has one electron, and tunnelling is allowed between dots to perform the projective spin-to-charge conversion readout. We refer to the spin states down(up) as $|0(1)\rangle$. In fact, our VQD supports any even number of qubits; the user specifies the desired number to determine the architecture (an even number of dots provides more practicality in practice). For instance, Figure 15 shows the six spin qubits in quantum dots used in our simulation.

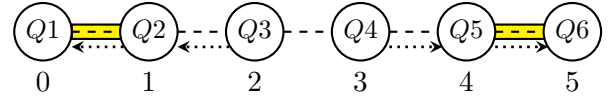


Figure 15: Architecture of six spin qubits in silicon quantum dots. Labels Q_j indicate the qubits aliases used in reference [77], while the numbers below represent qubit indices used in our VQD’s internal notation. The dashed lines indicate qubit connectivity for operating controlled-phase gates ($CPh(\theta)$). The dotted arrows indicate the direction of controlled- X gates ($CRot$), with the arrow pointing to the target qubit. The yellow rectangles indicate dot pairs that support direct parity readout, where output “1” indicates even parity and output “0” indicates odd parity. Measurement and initialisation of the middle qubits (Q_2, \dots, Q_5) are done indirectly.

Direct readout of qubits is only possible for the pair of edge qubits, where the obtained information is the parity of the two measured qubits. The parity measurement is realised via a projective measurement of the separated spin configuration to the joint singlet subspace: states with even parity 00 and 11 are not allowed to tunnel whereas the $|10\rangle$ and $|01\rangle$ do, in particular the $|01\rangle$ state via a fast decay. Moreover, the $|01\rangle$ decays (into $|10\rangle$) faster than the measurement timescale; such a protocol allows for a deterministic initialisation via real-time classical feedback. A measurement operation can be simulated by a projective measurement M , which projects a two-qubit state into the even and odd subspaces, followed by a Kraus map \mathcal{K} that simulates the decay of state $|01\rangle$.

The projective parity measurement M is de-

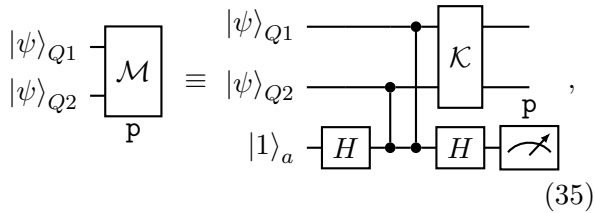
defined as

$$M = \{(|01\rangle\langle 01| + |10\rangle\langle 10|, \text{"0"}), (|00\rangle\langle 00| + |11\rangle\langle 11|, \text{"1"})\}, \quad (33)$$

where output "0" indicates detection of some change in current of a proximal detector, otherwise outputs "1". The Kraus map \mathcal{K} comprises operators K_j , where

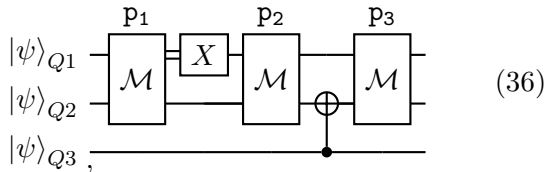
$$K = \{|00\rangle\langle 00|, |11\rangle\langle 11|, |10\rangle\langle 10|, |10\rangle\langle 01|\}, \quad (34)$$

and it fulfills $\sum_j K_j^\dagger K_j = I$. (Notice that the fourth element of K differs from the others: it maps $|01\rangle$ to $|10\rangle$.) Thus, the parity measurements, e.g., on qubits $Q1, Q2$ from Figure 15 is simulated by the following circuit



where qubit a indicates an ancillary qubit and $p \in \{\text{"0"}, \text{"1"}\}$ indicates parity measurement outcome of parity measurement projector \mathcal{M} (Equation (33)).

To measure the middle qubits, we apply the controlled- X ($CRot$) operation with the qubit of interest as controller, while employing the edge qubits as ancilla qubits; this is a form of quantum non-demolition (QND) measurement [108]. The following circuit achieves a QND measurement on $Q3$ and initialises qubits $Q1, Q2$ into state $|10\rangle$ at simultaneously [77]:



where p_3 is the outcome of measuring $Q3$ in the computational basis and the flip gate X is implemented conditioned on the classical bit p_1 . By performing another flip X to $Q3$ conditioned on the outcome p_3 followed by a repetition of the whole QND process, will result in deterministic initialisation of qubits $Q1, Q2$, and $Q3$ to state $|100\rangle$. By applying the same procedures to qubits $Q4, Q5$, and $Q6$, utilising measurement from the other end of the chain, we can achieve a deterministic full device initialisation into the state $|100001\rangle$.

The elementary single-qubit quantum operations on this platform comprise rotations $Rx(\theta)$ and $Ry(\theta)$, where θ is the rotation angle. Single qubit rotations can be implemented on each qubit. The rotation $Rz(\theta)$ can be implemented virtually (by adjusting the phase of the subsequent pulses).

The elementary two-qubit operations are controlled-phase gate ($CPh(\theta)_{i,j}$) and controlled- X gate ($CRot_{i,j}$). Controlled-phase gates can be implemented on any nearest neighbor qubits, as illustrated by the dashed lines in Figure 15. Controlled- X gates connectivity follows the dotted lines in Figure 15, with the target qubits indicated by the arrowhead.

7.3 Error models for our silicon spin VQD

The spin state readout \mathcal{M} that is shown in Equation (35) is the native measurement operator in our virtual silicon platform. Operator \mathcal{M} describes a two-qubit parity measurement accompanied with decay of state $|01\rangle$ to $|10\rangle$. The error of this measurement is modelled by two-qubit symmetric bit-flip error as described in Equation (16) that is applied before and after applying the measurement operator \mathcal{M} .

Single qubit rotations are susceptible to two types of errors. The first is the standard single-qubit error, for which error parameters are estimated using the method discussed in Appendix B.0.1. In this device, we assume that the error is dominated by the phase-flip error (Equation (3)). The second type of error arises from the off-resonant Rabi oscillation, where the value depends on the frequency detuning between the qubit that is operated upon and the ESR frequency utilised to drive the qubit that characterises each qubit.

The two-qubit phase gates mediated by the exchange interaction, such as CZ or $CPh(\theta)$, also experience two types of errors. Note that CZ gate is the same type of gate as $CPh(\theta)$ that is achieved by setting $\theta = \pi$. The first is the phase-flip error, as described in Equation (4). The second error is phase-flip cross-talk across the device associated with residual off-state exchange coupling, which is described by Z -rotation in Equation (8) and is dependent on rotation parameter θ . The strength of the cross-talk is characterised experimentally and varies across different pairs of qubits. For the conditional bit-flip ($CRot$), the

error is modelled by two-qubit depolarising noise as described in Equation (2).

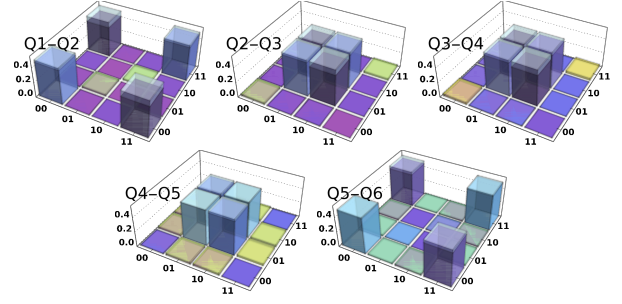
Passive qubits can experience free-induction exponential decays and weak phase-flip cross-talk. The exponential decays are characterised by the T_1 and T_2 time, which are described by Equation (13) and Equation (11), respectively. Weak dephasing cross-talk takes the form of conditional rotation, as described in Equation (8) and is characterised experimentally. This phase cross-talk is much stronger when operating a two-qubit phase gate such as CZ or $CPh(\theta)$. Here, we assume that the quantum gates are implemented in a serial manner, where the effect of passive noise can be more profound.

7.4 Bell states preparation on silicon qubits

In our virtual silicon qubits platform, we replicate a Bell pair generation experiment using different pairs of qubits, as recently achieved in [77]. We incorporate the reported experimental characteristics directly, and then the remaining parameters in the model are set through nonlinear optimisation based on the resulting Bell pair fidelities from the experiment. Remarkably, we are able to obtain very similar fidelities and output density matrices with a similar profile to the resulting tomography in the experiment.

The parameters we extract from the experiment detailed in [77] are summarized in Table 4 in the appendix. First, we incorporate their experimental parameters and noise estimation into our simulation to the greatest extent possible. Then, we optimize CZ gate fidelity with a cost function subject to the Bell state fidelities. We observe that CZ fidelities have a dominant influence on the resulting Bell pair fidelities. Finally, we obtain Figure 16, which shows the density matrix of the resulting Bell pairs and the optimized CZ fidelities.

Our optimisation process is based on the fidelity of the Bell pairs, which has allowed us to achieve a close match with the experimental results. Although some resulting concurrences are relatively poor, we have successfully obtained a density matrix profile similar to the tomography result in the experiment for most pairs. It is important to note that our density matrices are fetched from the exact emulation, so we do not need to consider errors acquired during the tomography process including shot noise. Overall,



Bell state fidelity(%) and concurrence (%) from the simulation and the experiment in [77] (Exp)

Qubits	Fid	Conc	Fid Exp	Conc Exp
Q1-Q2	89.40	79.75	89.2±2.2	86.7±3.2
Q2-Q3	90.18	80.42	90.1±2.2	83.9±3.8
Q3-Q4	88.71	79.08	88.3±3.6	87.9±5.0
Q4-Q5	95.97	94.49	95.6±2.0	94.9±3.2
Q5-Q6	94.26	90.59	94.1±1.4	90.6±3.6

Estimated fidelity (%) of CZ gates for each pair of qubits. Symbol μ indicates the average fidelity in the emulation and $\tilde{\mu}$ is the average fidelity in the experiment in [77].

Q1-Q2	Q2-Q3	Q3-Q4	Q4-Q5	Q5-Q6	μ	$\tilde{\mu}$
93.7	93.4	92.9	99.7	97.9	95.5	92

Figure 16: Emulation of Bell pair generation experiment in [77] on the Silicon qubit virtual device. An optimisation is performed over the fidelity of CZ (equivalently $CPh(\pi)$) gates subjected to the Bell pair generation fidelities in the experiment. The optimised value of the CZ fidelity is shown in the lower table. The estimated average fidelities of CZ operations is 95.5, higher than the estimated value in the experiment, namely 92. Using the optimised parameters, we plot the density matrix for each Bell pair overlapping with the noiseless case. The fidelity and concurrence of each Bell pair are shown in the upper table.

our results demonstrate that the VQD is a useful tool to estimate processor parameters from experimental data and could be utilised to guide the optimisation of Bell pair generation on a real device.

8 Superconducting qubits

8.1 Superconducting qubits physical system

Superconducting qubits [24, 49] are currently the most widely used and extensively studied solid-state qubits in the quantum computing community. They have been the subject of numerous advanced experiments, including the demonstration

of quantum advantage [6] and the implementation of NISQ (Noisy Intermediate-Scale Quantum) algorithms [46, 84].

Our superconducting qubits VQD is based on superconducting transmon qubits [50] that are connected by microwave resonators. A transmon qubit is a type of superconducting circuit consisting of a Josephson junction [45] and a capacitance, while the resonators provide a means for manipulating and reading out the qubits. In particular, our model is based on a class of devices developed at the University of Oxford [73, 79, 93].

In the circuit, the Josephson junction behaves as an oscillator, which can exhibit either linear or non-linear behaviour depending on its operating regime. When the junction is in its linear regime, it behaves like a simple harmonic oscillator. However, in the non-linear regime, the anharmonicity of the oscillator can be made sufficiently strong that we are able to regard the lowest two energy levels as a distinct two-level system: our qubit. Achieving high non-linearity is critical to prevent leakage and improve the selective manipulation and readout of the qubits.

8.2 Superconducting qubits architecture and native operations

In our VQD, the end-user can provide the fundamental characteristics of their superconducting qubits, which consist of qubit frequencies, anharmonicities, and the exchange coupling strengths of the resonators. The two-qubit ‘cross-resonance’ gates [59, 73, 91] have a directional preference; this comes from its nature using an asymmetric microwave drive (driving the control qubit at the target qubit frequency), while the preferred direction is determined by the qubit frequency and anharmonicity configurations. As an example, the connectivity layout of the virtual superconducting qubits in our simulation is illustrated in Figure 17.

Qubit initialisation must be executed at the beginning of the computation. Ideally, it sets all qubits to their ground state. In practice, most systems employ passive reset of superconducting circuits by waiting for an appropriate duration. During this process, the thermal bath from the surrounding environment is coupled with the qubits, allowing them to adiabatically reach thermal equilibrium, where some non-zero populations will reside in excited states.

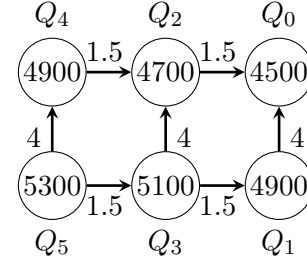


Figure 17: The layout of two-dimensional virtual six superconducting transmon qubits used in this simulation. The nodes correspond to transmon qubits and edges indicate capacitive coupling between the qubits. The numbers displayed on the nodes represent the frequencies of the qubits, whereas those on the edges correspond to the coupling strength. All frequency values are expressed in MHz, and the edges are directed towards the higher qubit frequencies, which dictate the preferred direction – for a faster operation – of the cross-resonance gate $ZX_{i,j}$, where qubit Q_i has a higher frequency than qubit Q_j ($Q_i \rightarrow Q_j$); in this case, we call Q_i as the control qubit and Q_j as the target qubit.

Qubit readout corresponds to measurement in the computational basis. It is assumed that the measurement process accounts for signal amplification and classification processes [21].

The set of physical single-qubit gates comprises $Rx(\theta)$, $Ry(\theta)$, and $Rz(\theta)$, where $\theta \in [-\pi, \pi]$. The $Rz(\theta)$ gate is considered to be implemented by the virtual (noiseless) Z rotation [63], which is accounted for in the phase of the subsequent pulse. In our model, the duration of physical single-qubit gates remains constant, irrespective of the variable θ . This approach mirrors the common practice in real physical devices, where an arbitrary rotation gate is implemented by modulating the signal amplitude while maintaining a fixed gate duration.

The set of native two-qubit gates comprises the cross-resonance gates and the siZZle (Stark-induced ZZ by level excursion) [103] gates:

$$ZX_{i,j} := e^{-i\frac{\pi}{2}Z_i \otimes X_j} \quad (37)$$

$$ZZ_{i,j} := e^{-i\frac{\pi}{2}Z_i \otimes Z_j}, \quad (38)$$

respectively, which are usually implemented as non-parameterised gates. The siZZle gate is a two-qubit gate that relies on off-resonant driving to induce an effective ZZ -interaction between qubits. Both gates can be parameterised by adjusting the amplitude and the driving pulse [46]; however, fixing the parameters is more com-

monly practised. Therefore, both gates are non-parameterised in this model.

8.3 Error models of superconducting qubits

The qubit initialisation operation will set the qubits' state into a product state of a statistical mixture of the ground state ($|0\rangle\langle 0|$) and excited state ($|1\rangle\langle 1|$), namely

$$\text{init}(\rho) = \bigotimes_j (p_j |0\rangle\langle 0|_j + (1 - p_j) |1\rangle\langle 1|_j) =: \rho_T, \quad (39)$$

where $1 - p_j$ is the probability associated with qubit Q_j being excited from the ground state. The resulting initialised state also corresponds to the thermal state ρ_T at a finite small temperature; one may initialise the qubits by leaving them for a sufficient amount of time, although active routes are also used [18, 29, 58, 82, 83].

Generalised amplitude damping $\text{gamp}(\Delta t)$ – associated with a duration Δt – is used to model T_1 -relaxation, which causes the state to relax towards its thermal state ρ_T (as described in Equation (39)). The action of $\text{gamp}(\Delta t)$ on a single-qubit density matrix ρ is described as follows

$$\begin{aligned} \rho &\mapsto \sum_{\alpha} \alpha \rho \alpha^{\dagger}, \\ \alpha &\in \left\{ \sqrt{p} \begin{pmatrix} 1 & 0 \\ 0 & \sqrt{1-\gamma} \end{pmatrix}, \sqrt{p} \begin{pmatrix} 0 & \sqrt{\gamma} \\ 0 & 0 \end{pmatrix}, \right. \\ &\quad \left. \sqrt{1-p} \begin{pmatrix} \sqrt{1-\gamma} & 0 \\ 0 & 1 \end{pmatrix}, \sqrt{1-p} \begin{pmatrix} 0 & 0 \\ \sqrt{\gamma} & 0 \end{pmatrix} \right\}, \end{aligned}$$

and $\gamma \equiv \gamma(\Delta t) = 1 - e^{-\Delta t/T_1}$,

(40)

where p is the probability of qubit population in state $|0\rangle\langle 0|$. Therefore, for a very long duration, at $\Delta t \rightarrow \infty$, the qubit will be in the statistical mixture of $p|0\rangle\langle 0| + (1 - p)|1\rangle\langle 1|$. On the other hand, the phase decoherence that is characterised by T_2 -relaxation, is modeled with dephasing noise, as described in Equation (11).

The qubit readout error is characterised by the T_1 -decay (Equation (40)) and depolarising noise (Equation (1)) that is models as

$$Q_j \text{---} \boxed{\text{gamp}(t_M)} \text{---} \boxed{\text{depol}(\varepsilon)} \text{---} \boxed{\text{0/1}} \text{---} \boxed{\text{depol}(\varepsilon)} \text{---}, \quad (41)$$

where t_M indicates the measurement duration and ε is infidelity of the measurement. The T_1

decay is considered in order to accurately capture the decay occurring during the measurement process, which often takes a significantly longer duration (approximately 100 times longer than gate applications). The measurement is sandwiched between depolarising operators, accounting for misclassification error that comes from the noise from the received signal, where the first operator impacts the classical outcome, while the second one introduces uncertainty to the projected state.

In this model, the logical operators can be implemented perfectly and fully in parallel. The errors arise solely from passive noise, which presents some complexity. The passive noise comprises free induction exponential decays characterised by T_1 and T_2 , as well as the residual ZZ -interactions from the static coupling along the capacitive coupling.

The capacitive coupling in a superconducting qubit system can enable multi-qubit operations and entanglement, but they can also introduce unwanted cross-talk. Specifically, in this model, we consider the static ZZ cross-talk that arises from an unintended or uncontrolled residual capacitive coupling between two qubits [66, 69].

If we denote the control qubit as c and the target qubit as t , the residual cross-talk is described as [51]

$$\exp(-i\beta Z \otimes Z), \quad \beta = J^2 \left(\frac{1}{\Delta_{ct} - \alpha_t} - \frac{1}{\Delta_{ct} + \alpha_c} \right), \quad (42)$$

where J is capacitive coupling strength, Δ_{ct} is the frequency difference between the qubits, and α_j is the anharmonicity of qubit j . In this model, we assume that we can adjust the ZZ interaction strength to the desired value perfectly, incorporating the fact that a static ZZ crosstalk exists; thus, the static ZZ cross-talk is completely mitigated when implementing a siZZle gate.

8.4 Variational Quantum Eigensolver on superconducting qubits

The variational Quantum Eigensolver (VQE) [75] is an promising route by which noisy-intermediate scale quantum (NISQ) devices may solve practical problems. Notably, the algorithms have been demonstrated to solve various small chemistry problems [19, 23, 30, 65, 72]. Such algorithms are ‘hybrid’, operating through a synergistic interplay between quantum and classical computers,

leveraging the strengths of both platforms. The achievable level of control on the quantum computer’s part is of course a crucial aspect. Superconducting qubit platforms typically exhibit a variety of gates each with a degree of adjustability, i.e., they are suitable as parameterised gates in VQEs. In the following, we demonstrate a VQE for solving the ground state of H_2 molecule using the six-qubit superconducting VQD as described above and shown in Figure 17.

The electronic Hamiltonian for the H_2 molecule is described using second quantisation, as follows:

$$H = \sum_{i,j} h_{ij} a_i^\dagger a_j + \sum_{i,j,k,l} h_{ijkl} a_i^\dagger a_j^\dagger a_k a_l, \quad (43)$$

where $\{a_j\}$ and $\{a_j^\dagger\}$ are the lowering and raising operators that act on a Fock space. Our choice of coefficients h_{ij} and h_{ijkl} represent the overlaps and exchange integrals of the contracted three Gaussian functions of the STO-3G [96] basis set, whose parameters are obtained via a self-consistent field procedure. Then, the Fock space is mapped into the qubit Hilbert space using the canonical Jordan-Wigner transformation [90, 104]. Finally, the Hamiltonian is expressed in the form of a Pauli sum,

$$H = \sum_k c_k P_k, \quad (44)$$

where $c_k \in \mathbb{R}$ and $P_k \in \{I, \sigma_x, \sigma_y, \sigma_z\}^{\otimes n}$ are n -qubit Pauli strings. We use the Python packages `Openfermion` [62] and `PyScf` [95] to generate the H_2 Hamiltonian that is expressed as a Pauli sum spanning qubits Q_0, Q_1, Q_2 , and Q_3 of Figure 17.

We use the VQE optimisation technique as described in [33]. The ansatz is constructed adaptively with the gate pool comprising native superconducting qubit operators (see Section 8.2) and with connectivity shown in Figure 17. The ansatz is iteratively refined, where in each iteration several intermediate ansätze are given, then the one with the lowest energy is chosen and simplified further by removing the superfluous gates. We use the natural gradient descent (also called imaginary-time evolution) method [61] to train our parameters. Finally, we execute the VQE on our virtual superconducting qubits device, with error parameters outlined in Table 5 in the appendix. The optimisation results are presented in Figure 18.

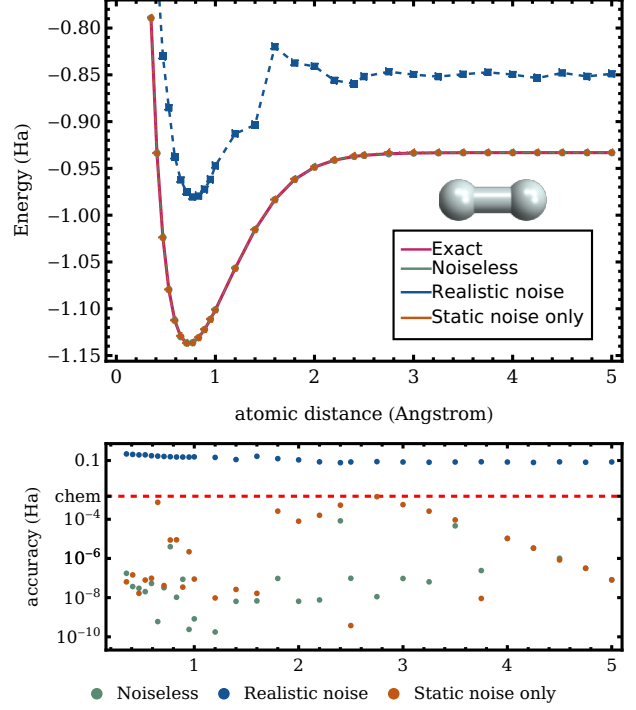


Figure 18: Estimations of ground state energies via VQE method (top) and the resulting accuracies (bottom), with the varying atomic distance of H_2 molecule. The unit of energy is Hartree, with chemical accuracy shown in the red dashed line. The optimisation has been shown to be successful with the given quantum computer architecture, as indicated by the *noiseless* line, which is aligned with the *exact* line. Moreover, the optimisation is capable of handling unitary static noise, as indicated by *static noise only* line. However, it fails when exposed to *realistic noise* setting.

Figure 18 shows that the output of the VQD deviates significantly from the ideal output because of the finite noise channels present. This is of course to be expected; generally, VQE studies have shown that precise (e.g., within ‘chemical accuracy’) results cannot be determined without incorporating a noise mitigation technique. Fortunately, however, such methods can make a dramatic improvement [46]. It would be natural to extend the VQD study we present here by examining the efficacy of different mitigation methods, such as zero-noise extrapolation, quasi-probability, and so forth [17]. However, it is interesting to note that deterministic errors are well-tolerated by VQEs since they represent a kind of systematic shift to parameters.

The six-qubit two-dimensional grid VQD described here does not correspond to any given reported experiment, but by making reasonable choices for the characteristics of the device we can

narrowly predict its performance. This illustrates the utility of the VQD platform as a kind of fast-prototyping tool – hardware teams can explore a range of systems and parameters in emulation in order to identify the most promising systems to actually fabricate.

9 Conclusion and further discussion

This paper has introduced the Virtual Quantum Device (VQD) tool and demonstrated its utility through a series of small studies – each focusing on a different form of quantum computing technology. We have explored ion traps in the context of remote Bell state generation, NV-centre type architectures as simulators for BCS models, stabiliser measurements in neutral atom devices, Bell state preparation in silicon spin systems, and VQE algorithms with superconducting systems. In each case, we have linked to either state-of-the-art experiments (replicating the results of those papers with a close fit) or recently proposed theoretical ideas and protocols.

These various demonstrations show that the VQD system is a valuable tool both for experimentalists wishing to understand data or test proposed designs, and for theorists who may want to explore ideas for algorithms and subroutines by testing them on a wide variety of platforms. Some of the studies are quite interesting investigations in their own right, and each of the VQDs that we created can straightforwardly be extended to match given physical devices even more closely.

10 Acknowledgements

The authors would like to express their gratitude to the following contributors for their valuable contributions to this work:

Mohammed Alghadeer, Mohamed Abobeih, Alessandro Ciani, Shuxiang Cao, Andrew Daley, Joseph Goodwin, Fernando Gonzalez-Zalba, Tomas Kozlej, Peter Leek, David Nadlinger, Natalie Pearson, Gerard Pelergi, Cody Poole, Jonathan Pritchard, Mark Saffman, Jason Smith, and Joanna Zajac.

The authors would like to acknowledge the use of the University of Oxford Advanced Research Computing (ARC) facility [81] in carrying out this work and specifically the facilities made available from the EPSRC QCS Hub grant (agree-

ment No. EP/T001062/1). CG is supported by this grant. The authors also acknowledge support from EPSRC's Robust and Reliable Quantum Computing (RoarQ) project (EP/W032635/1).

References

- [1] MH Abobeih, J Randall, CE Bradley, HP Bartling, MA Bakker, MJ Deegen, M Markham, DJ Twitchen, and TH Taminiau. Atomic-scale imaging of a 27-nuclear-spin cluster using a quantum sensor. *Nature*, 576(7787):411–415, 2019. DOI: [10.1038/s41586-019-1834-7](https://doi.org/10.1038/s41586-019-1834-7).
- [2] MH Abobeih, Y Wang, J Randall, SJH Loenen, CE Bradley, M Markham, DJ Twitchen, BM Terhal, and TH Taminiau. Fault-tolerant operation of a logical qubit in a diamond quantum processor. *Nature*, pages 1–1, 2022. DOI: [10.1038/s41586-022-04819-6](https://doi.org/10.1038/s41586-022-04819-6).
- [3] Mohamed Abobeih. *From atomic-scale imaging to quantum fault-tolerance with spins in diamond*. PhD thesis, Delft University of Technology, 2021.
- [4] Mohamed H Abobeih, Julia Cramer, Michiel A Bakker, Norbert Kalb, Matthew Markham, Daniel J Twitchen, and Tim H Taminiau. One-second coherence for a single electron spin coupled to a multi-qubit nuclear-spin environment. *Nature communications*, 9(1):2552, 2018. DOI: [10.1038/s41467-018-04916-z](https://doi.org/10.1038/s41467-018-04916-z).
- [5] Charles S Adams, Jonathan D Pritchard, and James P Shaffer. Rydberg atom quantum technologies. *Journal of Physics B: Atomic, Molecular and Optical Physics*, 53(1):012002, 2019. DOI: [10.1088/1361-6455/ab52ef](https://doi.org/10.1088/1361-6455/ab52ef).
- [6] Frank Arute, Kunal Arya, Ryan Babush, Dave Bacon, Joseph C Bardin, Rami Barends, Rupak Biswas, Sergio Boixo, Fernando GSL Brandao, David A Buell, et al. Quantum supremacy using a programmable superconducting processor. *Nature*, 574(7779):505–510, 2019. DOI: [10.5061/dryad.k6t1rj8](https://doi.org/10.5061/dryad.k6t1rj8).
- [7] C. J. Ballance, T. P. Harty, N. M. Linke, M. A. Sepiol, and D. M. Lucas. High-fidelity quantum logic gates using trapped-ion hyperfine qubits. *Phys. Rev. Lett.*, 117:

- 060504, Aug 2016. DOI: [10.1103/PhysRevLett.117.060504](https://doi.org/10.1103/PhysRevLett.117.060504).
- [8] Daniel Barredo, Sylvain De Léséleuc, Vincent Lienhard, Thierry Lahaye, and Antoine Browaeys. An atom-by-atom assembler of defect-free arbitrary two-dimensional atomic arrays. *Science*, 354(6315):1021–1023, 2016. DOI: [10.1126/science.aah3778](https://doi.org/10.1126/science.aah3778).
- [9] Daniel Barredo, Vincent Lienhard, Sylvain De Leseleuc, Thierry Lahaye, and Antoine Browaeys. Synthetic three-dimensional atomic structures assembled atom by atom. *Nature*, 561(7721):79–82, 2018. DOI: [10.1038/s41586-018-0450-2](https://doi.org/10.1038/s41586-018-0450-2).
- [10] MD Barrett, J Chiaverini, T Schaetz, J Britton, WM Itano, JD Jost, E Knill, C Langer, D Leibfried, R Ozeri, et al. Deterministic quantum teleportation of atomic qubits. *Nature*, 429(6993):737–739, 2004. DOI: [10.1088/1367-2630/10/1/013004](https://doi.org/10.1088/1367-2630/10/1/013004).
- [11] Sean D. Barrett and Pieter Kok. Efficient high-fidelity quantum computation using matter qubits and linear optics. *Phys. Rev. A*, 71:060310, Jun 2005. DOI: [10.1103/PhysRevA.71.060310](https://doi.org/10.1103/PhysRevA.71.060310).
- [12] Hannes Bernien. *Control, measurement and entanglement of remote quantum spin registers in diamond*. PhD thesis, Delft University of Technology, 2014.
- [13] II Beterov, IN Ashkarin, EA Yakshina, DB Tretyakov, VM Entin, II Ryabtsev, P Cheinet, P Pillet, and M Saffman. Fast three-qubit toffoli quantum gate based on three-body förster resonances in rydberg atoms. *Physical Review A*, 98(4):042704, 2018. DOI: [10.1103/PhysRevA.98.042704](https://doi.org/10.1103/PhysRevA.98.042704).
- [14] Dolev Bluvstein, Harry Levine, Giulia Semeghini, Tout T Wang, Sepehr Ebadi, Marcin Kalinowski, Alexander Keesling, Nishad Maskara, Hannes Pichler, Markus Greiner, et al. A quantum processor based on coherent transport of entangled atom arrays. *Nature*, 604(7906):451–456, 2022. DOI: [10.1038/s41586-022-04592-6](https://doi.org/10.1038/s41586-022-04592-6).
- [15] Conor E Bradley, Joe Randall, Mohamed H Abobeih, RC Berrevoets, MJ Degen, Michiel A Bakker, Matthew Markham, DJ Twitchen, and Tim H Taminiau. A ten-qubit solid-state spin register with quantum memory up to one minute. *Physical Review X*, 9(3):031045, 2019. DOI: [10.1103/PhysRevX.9.031045](https://doi.org/10.1103/PhysRevX.9.031045).
- [16] K. R. Brown, A. C. Wilson, Y. Colombe, C. Ospelkaus, A. M. Meier, E. Knill, D. Leibfried, and D. J. Wineland. Single-qubit-gate error below 10^{-4} in a trapped ion. *Phys. Rev. A*, 84:030303, Sep 2011. DOI: [10.1103/PhysRevA.84.030303](https://doi.org/10.1103/PhysRevA.84.030303).
- [17] Zhenyu Cai, Ryan Babbush, Simon C Benjamin, Suguru Endo, William J Huggins, Ying Li, Jarrod R McClean, and Thomas E O’Brien. Quantum error mitigation. *Reviews of Modern Physics*, 95(4):045005, 2023. DOI: [10.1103/RevModPhys.95.045005](https://doi.org/10.1103/RevModPhys.95.045005).
- [18] Shuxiang Cao, Mustafa Bakr, Giulio Campanaro, Simone D Fasciati, James Wills, Deep Lall, Boris Shteynas, Vivek Chandambaram, Ivan Rungger, and Peter Leek. Emulating two qubits with a four-level transmon qudit for variational quantum algorithms. *Quantum Science and Technology*, 9(3):035003, 2024. DOI: [10.1088/2058-9565/ad37d4](https://doi.org/10.1088/2058-9565/ad37d4).
- [19] Hans Hon Sang Chan, Nathan Fitzpatrick, Javier Segarra-Martí, Michael J Bearpark, and David P Tew. Molecular excited state calculations with adaptive wavefunctions on a quantum eigensolver emulation: reducing circuit depth and separating spin states. *Physical Chemistry Chemical Physics*, 23(46):26438–26450, 2021. DOI: [10.1039/D1CP02227J](https://doi.org/10.1039/D1CP02227J).
- [20] Juan I Cirac and Peter Zoller. Quantum computations with cold trapped ions. *Physical review letters*, 74(20):4091, 1995. DOI: [10.1103/PhysRevLett.74.4091](https://doi.org/10.1103/PhysRevLett.74.4091).
- [21] Aashish A Clerk, Michel H Devoret, Steven M Girvin, Florian Marquardt, and Robert J Schoelkopf. Introduction to quantum noise, measurement, and amplification. *Reviews of Modern Physics*, 82(2):1155, 2010. DOI: [10.1103/RevModPhys.82.1155](https://doi.org/10.1103/RevModPhys.82.1155).
- [22] Julia Cramer. *Quantum error correction with spins in diamond*. PhD thesis, Delft University of Technology, 12 2016.
- [23] Alain Delgado, Juan Miguel Arrazola, Soran Jahangiri, Zeyue Niu, Josh Izaac, Chase Roberts, and Nathan Killoran. Vari-

- ational quantum algorithm for molecular geometry optimization. *Physical Review A*, 104(5):052402, 2021. DOI: [10.1103/PhysRevA.104.052402](https://doi.org/10.1103/PhysRevA.104.052402).
- [24] Michel H Devoret, Andreas Wallraff, and John M Martinis. Superconducting qubits: A short review. *arXiv*, 2004. DOI: [10.48550/arXiv.cond-mat/0411174](https://doi.org/10.48550/arXiv.cond-mat/0411174).
- [25] P. Drmota, D. Main, D. P. Nadlinger, B.C. Nichol, M.A. Weber, E.M. Ainley, A. Agrawal, R. Srinivas, G. Araneda, C. J. Ballance, and D.M. Lucas. Robust quantum memory in a trapped-ion quantum network node. *Physical Review Letters*, 130(9), mar 2023. DOI: [10.1103/physrevlett.130.090803](https://doi.org/10.1103/physrevlett.130.090803).
- [26] Manuel Endres, Hannes Bernien, Alexander Keesling, Harry Levine, Eric R Anschuetz, Alexandre Krajenbrink, Crystal Senko, Vladan Vuletic, Markus Greiner, and Mikhail D Lukin. Atom-by-atom assembly of defect-free one-dimensional cold atom arrays. *Science*, 354(6315):1024–1027, 2016. DOI: [10.1126/science.aah3752](https://doi.org/10.1126/science.aah3752).
- [27] Simon J Evered, Dolev Bluvstein, Marcin Kalinowski, Sepehr Ebadi, Tom Manovitz, Hengyun Zhou, Sophie H Li, Alexandra A Geim, Tout T Wang, Nishad Maskara, et al. High-fidelity parallel entangling gates on a neutral-atom quantum computer. *Nature*, 622(7982):268–272, 2023. DOI: [10.1038/s41586-023-06481-y](https://doi.org/10.1038/s41586-023-06481-y).
- [28] Nicolai Friis, Oliver Marty, Christine Maier, Cornelius Hempel, Milan Holzäpfel, Petar Jurcevic, Martin B Plenio, Marcus Huber, Christian Roos, Rainer Blatt, et al. Observation of entangled states of a fully controlled 20-qubit system. *Physical Review X*, 8(2):021012, 2018. DOI: [10.1103/PhysRevX.8.021012](https://doi.org/10.1103/PhysRevX.8.021012).
- [29] Richard Gebauer, Nick Karcher, Daria Gusenkova, Martin Spiecker, Lukas Grünhaupt, Ivan Takmakov, Patrick Winkel, Luca Planat, Nicolas Roch, Wolfgang Wernsdorfer, et al. State preparation of a fluxonium qubit with feedback from a custom fpga-based platform. In *AIP Conference Proceedings*, volume 2241, page 020015. AIP Publishing LLC, 2020. DOI: [10.1063/5.0011721](https://doi.org/10.1063/5.0011721).
- [30] Harper R Grimsley, Sophia E Economou, Edwin Barnes, and Nicholas J Mayhall. An adaptive variational algorithm for exact molecular simulations on a quantum computer. *Nature communications*, 10(1):1–9, 2019. DOI: [10.1038/s41467-019-10988-2](https://doi.org/10.1038/s41467-019-10988-2).
- [31] Thomas Grurl, Jürgen Fuß, and Robert Wille. Noise-aware quantum circuit simulation with decision diagrams. *IEEE Transactions on Computer-Aided Design of Integrated Circuits and Systems*, 42(3):860–873, 2022. DOI: [10.1109/TCAD.2022.3182628](https://doi.org/10.1109/TCAD.2022.3182628).
- [32] Cica Gustiani. Virtual quantum device, 6 2023. URL <https://github.com/QTechTheory/VQD>.
- [33] Cica Gustiani, Richard Meister, and Simon C Benjamin. Exploiting subspace constraints and ab initio variational methods for quantum chemistry. *New Journal of Physics*, 25(7):073019, 2023. DOI: [10.1088/1367-2630/ace182](https://doi.org/10.1088/1367-2630/ace182).
- [34] T. P. Harty, D. T. C. Allcock, C. J. Ballance, L. Guidoni, H. A. Janacek, N. M. Linke, D. N. Stacey, and D. M. Lucas. High-fidelity preparation, gates, memory, and readout of a trapped-ion quantum bit. *Phys. Rev. Lett.*, 113:220501, Nov 2014. DOI: [10.1103/PhysRevLett.113.220501](https://doi.org/10.1103/PhysRevLett.113.220501).
- [35] Marc Hein, Jens Eisert, and Hans J Briegel. Multiparty entanglement in graph states. *Physical Review A*, 69(6):062311, 2004. DOI: [10.1103/PhysRevA.69.062311](https://doi.org/10.1103/PhysRevA.69.062311).
- [36] Creston D Herold, Spencer D Fallek, J True Merrill, Adam M Meier, Kenton R Brown, CE Volin, and Jason M Amini. Universal control of ion qubits in a scalable microfabricated planar trap. *New Journal of Physics*, 18(2):023048, 2016. DOI: [10.1088/1367-2630/18/2/023048](https://doi.org/10.1088/1367-2630/18/2/023048).
- [37] Michał Horodecki, Paweł Horodecki, and Ryszard Horodecki. General teleportation channel, singlet fraction, and quasidistillation. *Physical Review A*, 60(3):1888, 1999. DOI: [10.1103/PhysRevA.60.1888](https://doi.org/10.1103/PhysRevA.60.1888).
- [38] G Huber, T Deuschle, W Schnitzler, R Reichle, K Singer, and F Schmidt-Kaler. Transport of ions in a segmented linear paul trap in printed-circuit-board technology. *New Journal of Physics*, 10(1):013004, 2008. DOI: [10.1088/1367-2630/10/1/013004](https://doi.org/10.1088/1367-2630/10/1/013004).
- [39] P. Huft, Y. Song, T. M. Graham, K. Jooya,

- S. Deshpande, C. Fang, M. Kats, and M. Saffman. Simple, passive design for large optical trap arrays for single atoms. *Phys. Rev. A*, 105:063111, Jun 2022. DOI: [10.1103/PhysRevA.105.063111](https://doi.org/10.1103/PhysRevA.105.063111).
- [40] Larry Isenhower, Mark Saffman, and Klaus Mølmer. Multibit c k not quantum gates via rydberg blockade. *Quantum Information Processing*, 10:755–770, 2011. DOI: [10.1007/s11128-011-0292-4](https://doi.org/10.1007/s11128-011-0292-4).
- [41] Shreyans Jain, Tobias Sägesser, Pavel Hrmo, Celeste Torkzaban, Martin Stadler, Robin Oswald, Chris Axline, Amado Bautista-Salvador, Christian Ospelkaus, Daniel Kienzler, et al. Unit cell of a penning micro-trap quantum processor. *arXiv*, 2023. DOI: [10.48550/arXiv.2308.07672](https://doi.org/10.48550/arXiv.2308.07672).
- [42] Tyson Jones. Guide to creating device specifications, 6 2023. URL https://github.com/QTechTheory/QuESTlink/blob/main/Doc/guide_creating_device_spec.pdf.
- [43] Tyson Jones and Simon Benjamin. Questlink—mathematica embiggened by a hardware-optimised quantum emulator. *Quantum Science and Technology*, 5(3):034012, 2020. DOI: [10.1088/2058-9565/ab8506](https://doi.org/10.1088/2058-9565/ab8506).
- [44] Tyson Jones, Anna Brown, Ian Bush, and Simon C Benjamin. Quest and high performance simulation of quantum computers. *Scientific reports*, 9(1):1–11, 2019. DOI: [10.1038/s41598-019-47174-9](https://doi.org/10.1038/s41598-019-47174-9).
- [45] Brian David Josephson. Possible new effects in superconductive tunnelling. *Physics letters*, 1(7):251–253, 1962. DOI: [10.1016/0031-9163\(62\)91369-0](https://doi.org/10.1016/0031-9163(62)91369-0).
- [46] Abhinav Kandala, Antonio Mezzacapo, Kristan Temme, Maika Takita, Markus Brink, Jerry M Chow, and Jay M Gambetta. Hardware-efficient variational quantum eigensolver for small molecules and quantum magnets. *nature*, 549(7671):242–246, 2017. DOI: [10.1038/nature23879](https://doi.org/10.1038/nature23879).
- [47] Mohammadsadegh Khazali and Klaus Mølmer. Fast multiqubit gates by adiabatic evolution in interacting excited-state manifolds of rydberg atoms and superconducting circuits. *Physical Review X*, 10(2):021054, 2020. DOI: [10.1103/PhysRevX.10.021054](https://doi.org/10.1103/PhysRevX.10.021054).
- [48] David Kielpinski, Chris Monroe, and David J Wineland. Architecture for a large-scale ion-trap quantum computer. *Nature*, 417(6890):709–711, 2002. DOI: [10.1038/nature00784](https://doi.org/10.1038/nature00784).
- [49] Morten Kjaergaard, Mollie E Schwartz, Jochen Braumüller, Philip Krantz, Joel I-J Wang, Simon Gustavsson, and William D Oliver. Superconducting qubits: Current state of play. *Annual Review of Condensed Matter Physics*, 11:369–395, 2020. DOI: [10.1146/annurev-conmatphys-031119-050605](https://doi.org/10.1146/annurev-conmatphys-031119-050605).
- [50] Jens Koch, Terri M. Yu, Jay Gambetta, A. A. Houck, D. I. Schuster, J. Majer, Alexandre Blais, M. H. Devoret, S. M. Girvin, and R. J. Schoelkopf. Charge-insensitive qubit design derived from the cooper pair box. *Phys. Rev. A*, 76:042319, Oct 2007. DOI: [10.1103/PhysRevA.76.042319](https://doi.org/10.1103/PhysRevA.76.042319).
- [51] Philip Krantz, Morten Kjaergaard, Fei Yan, Terry P Orlando, Simon Gustavsson, and William D Oliver. A quantum engineer’s guide to superconducting qubits. *Applied physics reviews*, 6(2):021318, 2019. DOI: [10.1063/1.5089550](https://doi.org/10.1063/1.5089550).
- [52] V Krutyanskiy, M Galli, V Kremarsky, S Baier, DA Fioretto, Y Pu, A Mazloom, P Sekatski, M Canteri, M Teller, et al. Entanglement of trapped-ion qubits separated by 230 meters. *Physical Review Letters*, 130(5):050803, 2023. DOI: [10.1103/PhysRevLett.130.050803](https://doi.org/10.1103/PhysRevLett.130.050803).
- [53] Minh Kwon, Matthew F Ebert, Thad G Walker, and M Saffman. Parallel low-loss measurement of multiple atomic qubits. *Physical review letters*, 119(18):180504, 2017. DOI: [10.1103/PhysRevLett.119.180504](https://doi.org/10.1103/PhysRevLett.119.180504).
- [54] Harry Levine, Alexander Keesling, Giulia Semeghini, Ahmed Omran, Tout T Wang, Sepehr Ebadi, Hannes Bernien, Markus Greiner, Vladan Vuletić, Hannes Pichler, et al. Parallel implementation of high-fidelity multiqubit gates with neutral atoms. *Physical review letters*, 123(17):170503, 2019. DOI: [10.1103/PhysRevLett.123.170503](https://doi.org/10.1103/PhysRevLett.123.170503).
- [55] Ying Li and Simon C Benjamin. Efficient variational quantum simulator incorporating active error minimization. *Phys-*

- ical Review X*, 7(2):021050, 2017. DOI: [10.1103/PhysRevX.7.021050](https://doi.org/10.1103/PhysRevX.7.021050).
- [56] Daniel Loss and David P DiVincenzo. Quantum computation with quantum dots. *Physical Review A*, 57(1):120, 1998. DOI: [10.1103/PhysRevA.57.120](https://doi.org/10.1103/PhysRevA.57.120).
- [57] Mikhail D Lukin, Michael Fleischhauer, Robin Cote, LuMing Duan, Dieter Jaksch, J Ignacio Cirac, and Peter Zoller. Dipole blockade and quantum information processing in mesoscopic atomic ensembles. *Physical review letters*, 87(3):037901, 2001. DOI: [10.1103/PhysRevLett.87.037901](https://doi.org/10.1103/PhysRevLett.87.037901).
- [58] Paul Magnard, Philipp Kurpiers, Baptiste Royer, Theo Walter, J-C Besse, Simone Gasparinetti, Marek Pechal, Johannes Heinsoo, Simon Storz, Alexandre Blais, et al. Fast and unconditional all-microwave reset of a superconducting qubit. *Physical review letters*, 121(6):060502, 2018. DOI: [10.1103/PhysRevLett.121.060502](https://doi.org/10.1103/PhysRevLett.121.060502).
- [59] Moein Malekakhlagh, Easwar Magesan, and David C McKay. First-principles analysis of cross-resonance gate operation. *Physical Review A*, 102(4):042605, 2020. DOI: [10.1103/PhysRevA.102.042605](https://doi.org/10.1103/PhysRevA.102.042605).
- [60] M. Malinowski, D.T.C. Allcock, and C.J. Ballance. How to wire a 1000-qubit trapped-ion quantum computer. *PRX Quantum*, 4:040313, Oct 2023. DOI: [10.1103/PRXQuantum.4.040313](https://doi.org/10.1103/PRXQuantum.4.040313).
- [61] Sam McArdle, Tyson Jones, Suguru Endo, Ying Li, Simon C Benjamin, and Xiao Yuan. Variational ansatz-based quantum simulation of imaginary time evolution. *npj Quantum Information*, 5(1):1–6, 2019. DOI: [10.1038/s41534-019-0187-2](https://doi.org/10.1038/s41534-019-0187-2).
- [62] Jarrod R McClean, Nicholas C Rubin, Kevin J Sung, Ian D Kivlichan, Xavier Bonet-Monroig, Yudong Cao, Chengyu Dai, E Schuyler Fried, Craig Gidney, Brendan Gimby, et al. Openfermion: the electronic structure package for quantum computers. *Quantum Science and Technology*, 5(3):034014, 2020. DOI: [10.1088/2058-9565/ab8ebc](https://doi.org/10.1088/2058-9565/ab8ebc).
- [63] David C McKay, Christopher J Wood, Sarah Sheldon, Jerry M Chow, and Jay M Gambetta. Efficient z gates for quantum computing. *Physical Review A*, 96(2):022330, 2017. DOI: [10.1103/PhysRevA.96.022330](https://doi.org/10.1103/PhysRevA.96.022330).
- [64] Richard Meister, Cica Gustiani, and Simon C Benjamin. Exploring ab initio machine synthesis of quantum circuits. *New Journal of Physics*, 25(7):073018, 2023. DOI: [10.1088/1367-2630/ace077](https://doi.org/10.1088/1367-2630/ace077).
- [65] Mekena Metcalf, Nicholas P Bauman, Karol Kowalski, and Wibe A De Jong. Resource-efficient chemistry on quantum computers with the variational quantum eigensolver and the double unitary coupled-cluster approach. *Journal of chemical theory and computation*, 16(10):6165–6175, 2020. DOI: [10.1021/acs.jctc.0c00421](https://doi.org/10.1021/acs.jctc.0c00421).
- [66] Bradley K Mitchell, Ravi K Naik, Alexis Morvan, Akel Hashim, John Mark Kreikebaum, Brian Marinelli, Wim Lavrijsen, Kasra Nowrouzi, David I Santiago, and Irfan Siddiqi. Hardware-efficient microwave-activated tunable coupling between superconducting qubits. *Physical review letters*, 127(20):200502, 2021. DOI: [10.1103/PhysRevLett.127.200502](https://doi.org/10.1103/PhysRevLett.127.200502).
- [67] M. Morgado and S. Whitlock. Quantum simulation and computing with Rydberg-interacting qubits. *AVS Quantum Science*, 3(2), 05 2021. ISSN 2639-0213. DOI: [10.1116/5.0036562](https://doi.org/10.1116/5.0036562). 023501.
- [68] S. A. Moses, C. H. Baldwin, M. S. Allman, R. Ancona, L. Ascarrunz, C. Barnes, J. Bartolotta, B. Bjork, P. Blanchard, M. Bohn, J. G. Bohnet, N. C. Brown, N. Q. Burdick, W. C. Burton, S. L. Campbell, J. P. Campora, C. Carron, J. Chambers, J. W. Chan, Y. H. Chen, A. Chernoguzov, E. Chertkov, J. Colina, J. P. Curtis, R. Daniel, M. DeCross, D. Deen, C. Delaney, J. M. Dreiling, C. T. Ertsgaard, J. Esposito, B. Estey, M. Fabrikant, C. Figgatt, C. Foltz, M. Foss-Feig, D. Francois, J. P. Gaebler, T. M. Gatterman, C. N. Gilbreth, J. Giles, E. Glynn, A. Hall, A. M. Hankin, A. Hansen, D. Hayes, B. Higashi, I. M. Hoffman, B. Horning, J. J. Hout, R. Jacobs, J. Johansen, L. Jones, J. Karcz, T. Klein, P. Lauria, P. Lee, D. Liefer, S. T. Lu, D. Lucchetti, C. Lytle, A. Malm, M. Matheny, B. Mathewson, K. Mayer, D. B. Miller, M. Mills, B. Neyenhuis, L. Nugent, S. Olson, J. Parks, G. N. Price,

- Z. Price, M. Pugh, A. Ransford, A. P. Reed, C. Roman, M. Rowe, C. Ryan-Anderson, S. Sanders, J. Sedlacek, P. Shevchuk, P. Siegfried, T. Skripka, B. Spaun, R. T. Sprenkle, R. P. Stutz, M. Swallows, R. I. Tobey, A. Tran, T. Tran, E. Vogt, C. Volin, J. Walker, A. M. Zolot, and J. M. Pino. A race-track trapped-ion quantum processor. *Phys. Rev. X*, 13:041052, Dec 2023. DOI: [10.1103/PhysRevX.13.041052](https://doi.org/10.1103/PhysRevX.13.041052).
- [69] Pranav Mundada, Gengyan Zhang, Thomas Hazard, and Andrew Houck. Suppression of qubit crosstalk in a tunable coupling superconducting circuit. *Physical Review Applied*, 12(5):054023, 2019. DOI: [10.1103/PhysRevApplied.12.054023](https://doi.org/10.1103/PhysRevApplied.12.054023).
- [70] Michael A Nielsen. A simple formula for the average gate fidelity of a quantum dynamical operation. *Physics Letters A*, 303(4):249–252, 2002. DOI: [10.1016/S0375-9601\(02\)01272-0](https://doi.org/10.1016/S0375-9601(02)01272-0).
- [71] Boyko Nikolov, Elliot Diamond-Hitchcock, Jonathan Bass, NLR Spong, and JD Pritchard. Randomized benchmarking using nondestructive readout in a two-dimensional atom array. *Physical Review Letters*, 131(3):030602, 2023. DOI: [10.1103/PhysRevLett.131.030602](https://doi.org/10.1103/PhysRevLett.131.030602).
- [72] Pauline J Ollitrault, Alberto Baiardi, Markus Reiher, and Ivano Tavernelli. Hardware efficient quantum algorithms for vibrational structure calculations. *Chemical science*, 11(26):6842–6855, 2020. DOI: [10.1039/D0SC01908A](https://doi.org/10.1039/D0SC01908A).
- [73] AD Patterson, J Rahamim, T Tsunoda, PA Spring, S Jebari, K Ratter, M Mergenthaler, G Tancredi, B Vlastakis, M Esposito, et al. Calibration of a cross-resonance two-qubit gate between directly coupled transmons. *Physical Review Applied*, 12(6):064013, 2019. DOI: [10.1103/PhysRevApplied.12.064013](https://doi.org/10.1103/PhysRevApplied.12.064013).
- [74] Wolfgang Paul. Electromagnetic traps for charged and neutral particles. *Reviews of modern physics*, 62(3):531, 1990. DOI: [10.1103/RevModPhys.62.531](https://doi.org/10.1103/RevModPhys.62.531).
- [75] Alberto Peruzzo, Jarrod McClean, Peter Shadbolt, Man-Hong Yung, Xiao-Qi Zhou, Peter J Love, Alán Aspuru-Guzik, and Jeremy L O’Brien. A variational eigenvalue solver on a photonic quantum processor. *Nature communications*, 5(1):1–7, 2014. DOI: [10.1038/ncomms5213](https://doi.org/10.1038/ncomms5213).
- [76] David Petrosyan, Felix Motzoi, Mark Saffman, and Klaus Mølmer. High-fidelity rydberg quantum gate via a two-atom dark state. *Physical Review A*, 96(4):042306, 2017. DOI: [10.1103/PhysRevA.96.042306](https://doi.org/10.1103/PhysRevA.96.042306).
- [77] Stephan GJ Philips, Mateusz T Maździk, Sergey V Amitonov, Sander L de Snoo, Maximilian Russ, Nima Kalhor, Christian Volk, William IL Lawrie, Delphine Brousse, Larysa Tryputen, et al. Universal control of a six-qubit quantum processor in silicon. *Nature*, 609(7929):919–924, 2022. DOI: [10.1038/s41586-022-05117-x](https://doi.org/10.1038/s41586-022-05117-x).
- [78] Juan M Pino, Jennifer M Dreiling, Caroline Figgatt, John P Gaebler, Steven A Moses, MS Allman, CH Baldwin, Michael Foss-Feig, D Hayes, K Mayer, et al. Demonstration of the trapped-ion quantum ccd computer architecture. *Nature*, 592(7853):209–213, 2021. DOI: [10.1038/s41586-021-03318-4](https://doi.org/10.1038/s41586-021-03318-4).
- [79] J Rahamim, T Behrle, MJ Peterer, A Patterson, PA Spring, T Tsunoda, R Marenti, G Tancredi, and PJ Leek. Double-sided coaxial circuit qed with out-of-plane wiring. *Applied Physics Letters*, 110(22):222602, 2017. DOI: [10.1063/1.4984299](https://doi.org/10.1063/1.4984299).
- [80] SE Rasmussen, K Groenland, R Gerritsma, K Schoutens, and NT Zinner. Single-step implementation of high-fidelity n-bit toffoli gates. *Physical Review A*, 101(2):022308, 2020. DOI: [10.1103/PhysRevA.101.022308](https://doi.org/10.1103/PhysRevA.101.022308).
- [81] Andrew Richards. University of oxford advanced research computing. *Zenodo*, Aug 2015. DOI: [10.5281/zenodo.22558](https://doi.org/10.5281/zenodo.22558).
- [82] D Ristè, CC Bultink, Konrad W Lehnert, and L DiCarlo. Feedback control of a solid-state qubit using high-fidelity projective measurement. *Physical review letters*, 109(24):240502, 2012. DOI: [10.1103/PhysRevLett.109.240502](https://doi.org/10.1103/PhysRevLett.109.240502).
- [83] Diego Ristè, Josephine G van Leeuwen, H-S Ku, Konrad W Lehnert, and Leonardo DiCarlo. Initialization by measurement of a superconducting quantum bit circuit. *Physical review letters*, 109(5):050507, 2012. DOI: [10.1103/PhysRevLett.109.050507](https://doi.org/10.1103/PhysRevLett.109.050507).
- [84] Diego Riste, Marcus P Da Silva, Colm A Ryan, Andrew W Cross, Antonio D Cór-

- coles, John A Smolin, Jay M Gambetta, Jerry M Chow, and Blake R Johnson. Demonstration of quantum advantage in machine learning. *npj Quantum Information*, 3(1):16, 2017. DOI: [10.1038/s41534-017-0017-3](https://doi.org/10.1038/s41534-017-0017-3).
- [85] Lucio Robledo, Lilian Childress, Hannes Bernien, Bas Hensen, Paul FA Alkemade, and Ronald Hanson. High-fidelity projective read-out of a solid-state spin quantum register. *Nature*, 477(7366):574–578, 2011. DOI: [10.1038/nature10401](https://doi.org/10.1038/nature10401).
- [86] Jannis Ruh, Regina Finsterhoelzl, and Guido Burkard. Digital quantum simulation of the bcs model with a central-spin-like quantum processor. *Physical Review A*, 107(6):062604, 2023. DOI: [10.1103/PhysRevA.107.062604](https://doi.org/10.1103/PhysRevA.107.062604).
- [87] Mark Saffman. Quantum computing with atomic qubits and rydberg interactions: progress and challenges. *Journal of Physics B: Atomic, Molecular and Optical Physics*, 49(20):202001, 2016. DOI: [0953-4075/49/20/202001](https://doi.org/10.1088/0953-4075/49/20/202001).
- [88] Ludwig Schmid, David F Locher, Manuel Rispler, Sebastian Blatt, Johannes Zeiher, Markus Müller, and Robert Wille. Computational capabilities and compiler development for neutral atom quantum processors—connecting tool developers and hardware experts. *Quantum Science and Technology*, 9(3):033001, 2024. DOI: [10.1103/10.1088/2058-9565/ad33ac](https://doi.org/10.1103/10.1088/2058-9565/ad33ac).
- [89] Amanda E Seedhouse, Tuomo Tantt, Ross CC Leon, Ruichen Zhao, Kuan Yen Tan, Bas Hensen, Fay E Hudson, Kohei M Itoh, Jun Yoneda, Chih Hwan Yang, et al. Pauli blockade in silicon quantum dots with spin-orbit control. *PRX Quantum*, 2(1):010303, 2021. DOI: [10.1103/PRXQuantum.2.010303](https://doi.org/10.1103/PRXQuantum.2.010303).
- [90] Jacob T Seeley, Martin J Richard, and Peter J Love. The bravyi-kitaev transformation for quantum computation of electronic structure. *The Journal of chemical physics*, 137(22):224109, 2012. DOI: [10.1063/1.4768229](https://doi.org/10.1063/1.4768229).
- [91] Sarah Sheldon, Easwar Magesan, Jerry M Chow, and Jay M Gambetta. Procedure for systematically tuning up cross-talk in the cross-resonance gate. *Physical Review A*, 93(6):060302, 2016. DOI: [10.1103/PhysRevA.93.060302](https://doi.org/10.1103/PhysRevA.93.060302).
- [92] Anders Sørensen and Klaus Mølmer. Quantum computation with ions in thermal motion. *Phys. Rev. Lett.*, 82:1971–1974, Mar 1999. DOI: [10.1103/PhysRevLett.82.1971](https://doi.org/10.1103/PhysRevLett.82.1971).
- [93] Peter A Spring, Shuxiang Cao, Takahiro Tsunoda, Giulio Campanaro, Simone Fasciati, James Wills, Mustafa Bakr, Vivek Chidambaram, Boris Shteynas, Lewis Carpenter, et al. High coherence and low cross-talk in a tileable 3d integrated superconducting circuit architecture. *Science Advances*, 8(16):eabl6698, 2022. DOI: [10.1126/sciadv.abl6698](https://doi.org/10.1126/sciadv.abl6698).
- [94] L. J. Stephenson, D. P. Nadlinger, B. C. Nichol, S. An, P. Drmota, T. G. Ballance, K. Thirumalai, J. F. Goodwin, D. M. Lucas, and C. J. Ballance. High-rate, high-fidelity entanglement of qubits across an elementary quantum network. *Phys. Rev. Lett.*, 124:110501, Mar 2020. DOI: [10.1103/PhysRevLett.124.110501](https://doi.org/10.1103/PhysRevLett.124.110501).
- [95] Qiming Sun, Timothy C Berkelbach, Nick S Blunt, George H Booth, Sheng Guo, Zhen-dong Li, Junzi Liu, James D McClain, Elvira R Sayfutyarova, Sandeep Sharma, et al. Pyscf: the python-based simulations of chemistry framework. *Wiley Interdisciplinary Reviews: Computational Molecular Science*, 8(1):e1340, 2018. DOI: [10.1002/wcms.1340](https://doi.org/10.1002/wcms.1340).
- [96] Attila Szabo and Neil S Ostlund. *Modern quantum chemistry: introduction to advanced electronic structure theory*. Courier Corporation, 2012. ISBN 9780486691862.
- [97] Tim Hugo Tamini, Julia Cramer, Toeno van der Sar, Viatcheslav V Dobrovitski, and Ronald Hanson. Universal control and error correction in multi-qubit spin registers in diamond. *Nature nanotechnology*, 9(3):171–176, 2014. DOI: [10.1038/nnano.2014.2](https://doi.org/10.1038/nnano.2014.2).
- [98] Kristan Temme, Sergey Bravyi, and Jay M Gambetta. Error mitigation for short-depth quantum circuits. *Physical review letters*, 119(18):180509, 2017. DOI: [10.1103/PhysRevLett.119.180509](https://doi.org/10.1103/PhysRevLett.119.180509).
- [99] LS Theis, F Motzoi, FK Wilhelm, and M Saffman. High-fidelity rydberg-blockade entangling gate using shaped, analytic

- pulses. *Physical Review A*, 94(3):032306, 2016. DOI: [10.1103/PhysRevA.94.032306](https://doi.org/10.1103/PhysRevA.94.032306).
- [100] E Urban, Todd A Johnson, T Henage, L Isenhower, DD Yavuz, TG Walker, and M Saffman. Observation of rydberg blockade between two atoms. *Nature Physics*, 5(2):110–114, 2009. DOI: [10.1038/nphys1183](https://doi.org/10.1038/nphys1183).
- [101] Lieven MK Vandersypen and Mark A Eriksson. with semiconductor spins. *Physics Today*, 72:8–38, 2019. DOI: [10.1063/PT.3.4270](https://doi.org/10.1063/PT.3.4270).
- [102] Yang Wang, Aishwarya Kumar, Tsung-Yao Wu, and David S Weiss. Single-qubit gates based on targeted phase shifts in a 3d neutral atom array. *Science*, 352(6293):1562–1565, 2016. DOI: [10.1126/science.aaf2581](https://doi.org/10.1126/science.aaf2581).
- [103] KX Wei, Easwar Magesan, Isaac Lauer, S Srinivasan, Daniela F Bogorin, S Carnevale, GA Keefe, Y Kim, D Klaus, W Landers, et al. Hamiltonian engineering with multicolor drives for fast entangling gates and quantum crosstalk cancellation. *Physical Review Letters*, 129(6):060501, 2022. DOI: [10.1103/PhysRevLett.129.060501](https://doi.org/10.1103/PhysRevLett.129.060501).
- [104] E Wigner and Pascual Jordan. Über das paulische äquivalenzverbot. *Z. Phys*, 47: 631, 1928. DOI: [10.1007/BF01331938](https://doi.org/10.1007/BF01331938).
- [105] Yukai Wu, Sheng-Tao Wang, and L-M Duan. Noise analysis for high-fidelity quantum entangling gates in an anharmonic linear paul trap. *Physical Review A*, 97(6):062325, 2018. DOI: [10.1103/PhysRevA.97.062325](https://doi.org/10.1103/PhysRevA.97.062325).
- [106] T Xia, M Lichtman, K Maller, AW Carr, MJ Piotrowicz, L Isenhower, and M Saffman. Randomized benchmarking of single-qubit gates in a 2d array of neutral-atom qubits. *Physical review letters*, 114(10):100503, 2015. DOI: [10.1103/PhysRevLett.114.100503](https://doi.org/10.1103/PhysRevLett.114.100503).
- [107] Xiangkun Xu, Zixiang Wang, Changkui Duan, Pu Huang, Pengfei Wang, Ya Wang, Nanyang Xu, Xi Kong, Fazhan Shi, Xing Rong, et al. Coherence-protected quantum gate by continuous dynamical decoupling in diamond. *Physical review letters*, 109(7):070502, 2012. DOI: [10.1103/PhysRevLett.109.070502](https://doi.org/10.1103/PhysRevLett.109.070502).
- [108] Jun Yoneda, Kenta Takeda, Tomohiro Otsuka, Takashi Nakajima, Matthieu R Delbecq, Giles Allison, Takumu Honda, Tetsuo Koderu, Shunri Oda, Yusuke Hoshi, et al. A quantum-dot spin qubit with coherence limited by charge noise and fidelity higher than 99.9%. *Nature nanotechnology*, 13(2): 102–106, 2018. DOI: [10.1038/s41565-017-0014-x](https://doi.org/10.1038/s41565-017-0014-x).

A Design philosophy and choice of QuESTlink

As noted in Section 2 of the main paper, there are a number of considerations that must inform the choice of which platform on which to base the VQD framework. We selected QuESTlink, because of its combination of the QuEST emulator (a fully featured and performant emulator) with the powerful symbolic manipulation capabilities of the commercial product Mathematica. Here we explain this choice and its benefits, both to expert users who will create new VQDs, and also for making our task of creating the VQD framework as tractable as possible.

We noted that there are a number of potential pain points for the task of defining a new VQD. It requires describing the imperfect experimental processes, whether through canonical noise channels (like dephasing and depolarising) or more generally as Kraus maps, potentially requiring laborious tomography. Encoding the nuances of a real-time device into a dichotomy of active and passive, discrete noise processes can be a significant challenge for an experimentalist, and may require duplicated efforts to model unique devices of the same general platform (such as separate superconducting experiments). Further, it is often preferable to describe a device through a platform-native language (for instance, borrowing the language of superconducting experiments) and to model a device as a time-dependent object with its own internal states, rather than a static map between circuits and channels.

The virtual quantum device package must address these pain points. It provides a high-level and experimental platform-specific interface for generating device specifications, where standard physical properties such as coherence times and coupling strengths become user-variable parameters. In essence, the user configures a hardware platform in its native language and bespoke parameters, and the VQD generates a QuESTlink device specification in the language of digital gates and channels.

These capabilities are achieved by making extensive use of Mathematica’s functional, symbolic and pattern-matching facilities. This significantly reduces the necessary code, and simplifies the software architecture, from a transpiler written in non-symbolic languages like Python or C. As a contrived example, consider the Mathematica snippet below:

```
u /. C_{c_/,c<3} [(X|Y|Z)_{t_/,t>=3}] /; (Abs[t-c] >= 2)
      :> Depol_{c,t} [15/16(1-Exp[-t])]
```

While it may appear opaque to users unfamiliar with Mathematica, this short sequence performs a rather complex task with only 71 keystrokes: It modifies the given QuESTlink circuit `u` (a list of symbolic gates) by replacing all controlled-Pauli gates which control upon the first 3 qubits, and which target the remaining qubits excluding that adjacent to the control, with a two-qubit depolarising channel upon the same qubits with a target-dependent error probability. While this is an entirely artificial example, it showcases the expressibility of Mathematica and its utility for transpiling circuits.

The VQD produces device specifications which can be subsequently passed to QuESTlink functions like `InsertCircuitNoise` in order to translate ideal circuits into realistic channels, expressed as a sequence of unitary and decohering operators. This sequence can then be exported, or effected upon a quantum state simulated with QuESTlink via functions like `ApplyCircuit`. As noted in the main paper, all this applies both to state vectors and to density matrices according to the users preference, and this choice can be switched trivially from one to the other.

B Inferring the severity of depolarising and dephasing noise

Most reported gate fidelities in experiments come from random quantum state benchmarking. Ideally, one measures the average fidelities over Haar-distributed random quantum states. Using the results of references [37, 70], one can estimate the error parameter for depolarising and dephasing channels (see Section 3.1) given its average fidelity. Note that in this section, we only consider one- and two-qubit gates.

Let \mathcal{E} a CPTP map describing errors of quantum gate U ; both operators are acting on Hilbert space \mathcal{H} , which has a dimension d . The *average fidelity* \bar{F} of map \mathcal{E} is defined as

$$\bar{F}(\mathcal{E}) \equiv \int d\psi \langle \psi | \mathcal{E}(\rho) | \psi \rangle, \quad (45)$$

where $\rho = |\psi\rangle\langle\psi|$, $\rho \in \mathcal{H}$, and the integral is normalised and evaluated over the uniform (Haar) measure $d\psi$ on state space \mathcal{H} . Let the noisy form of the gate U be $U_{\mathcal{E}} \equiv \mathcal{E}(U)$, then the average fidelity of gate U can be estimated by applying U^\dagger to random states $|\psi\rangle$, followed with $U_{\mathcal{E}}$,

$$\bar{F}(\mathcal{E}) = \bar{F}(U_{\mathcal{E}}, U) = \int d\psi \langle \psi | U_{\mathcal{E}}(U\rho U^\dagger) | \psi \rangle, \quad (46)$$

where the perfect fidelity is obtained when \mathcal{E} is an identity operation. Second, the *entanglement fidelity* of map \mathcal{E} is defined as

$$F_e(\mathcal{E}) \equiv \langle \Phi | (\mathcal{E} \otimes \mathcal{I})(\rho_\Phi) | \Phi \rangle, \quad (47)$$

where $\rho_\Phi \in \mathcal{H} \otimes \mathcal{H}$, $\rho_\Phi = |\Phi\rangle\langle\Phi|$, and $|\Phi\rangle = \frac{1}{\sqrt{d}} \sum_{j=0}^{d-1} |jj\rangle$ is a maximally entangled state, and \mathcal{I} an identity operator acting on \mathcal{H} .

The entanglement fidelity of noisy gate $U_{\mathcal{E}}$ can be obtained as follows

$$F_e(\mathcal{E}) = F_e(U_{\mathcal{E}}, U) = \langle \Phi | (U_{\mathcal{E}} \otimes \mathcal{I})(U\rho_\Phi U^\dagger) | \Phi \rangle, \quad (48)$$

where U is acting on the first half of the registers containing ρ .

Obtaining $F_e(\mathcal{E})$ is more straightforward than $\bar{F}(\mathcal{E})$. Using Horodecki et al.'s equation, we obtain the average fidelity given the entanglement fidelity [37]:

$$\bar{F}(\mathcal{E}) = \frac{dF_e(\mathcal{E}) + 1}{d + 1}, \quad (49)$$

where d is the dimension of \mathcal{H} . Using this formula, we reverse-engineer the noisy gate given an average fidelity \bar{F} that is obtained by random state benchmarking in the experiment. We refer to [37, 70] for further details on this fidelities relation.

B.0.1 One-qubit gate error parameter estimate

Let $U_{\mathcal{E}}$ be a noisy single unitary matrix in which the error $\mathcal{E}_{p,q}$ admits decomposition as in Equation (6). First, we calculate entanglement fidelity

$$F_e = \langle \Phi^+ | (\mathcal{E}_{p,q} \otimes \mathcal{I})(\rho) | \Phi^+ \rangle, \quad (50)$$

where $|\Phi^+\rangle = (|00\rangle + |11\rangle)/\sqrt{2}$ and $\rho = |\Phi^+\rangle\langle\Phi^+|$. Evaluating the value while keeping p and q as free (error) parameters gives us

$$F_e = 1 - p - q + \frac{4}{3}pq. \quad (51)$$

In practice, we want the capability to adjust the severity of depolarising and dephasing errors. So now, we introduce $x \in [0, 1]$ as a fraction describing depolarising versus dephasing, where $x = 1$ indicates completely depolarising, and $x = 0$ signifies entirely dephasing. Thus, we solve

$$1 - p(1 - x) - qx + \frac{4}{3}pqx(1 - x) = \frac{3\bar{F} - 1}{2} \quad (52)$$

to estimate p and q , where \bar{F} is the reported one-qubit gate fidelity in the experiment.

B.0.2 Two-qubit gate error parameter estimate

If $U_{\mathcal{E}}$ is a two-qubit gate, we start with two pairs of Bell states $\rho = |\Phi^+\Phi^+\rangle\langle\Phi^+\Phi^+|_{p,r,q,s}$. Entanglement fidelity is defined as the fidelity of the initial state after the application of the standard two-qubit noise $\mathcal{E}_{p,q}$,

$$F_e = \langle\Phi^+\Phi^+|(\mathcal{E}_{p,q} \otimes \mathcal{I})(\rho)|\Phi^+\Phi^+\rangle_{p,r,q,s}, \quad (53)$$

where the error $\mathcal{E}_{p,q}$ is composed of two-qubit depolarising noise (Equation (2)) and two-qubit dephasing noise (Equation (4)). Then, we obtain the quantity

$$F_e = 1 - p - q + \frac{16}{15}pq. \quad (54)$$

Introducing error fraction (depolarising versus dephasing) $x \in [0, 1]$ to the equation, we solve

$$1 - p(1 - x) - qx + \frac{16}{15}pqx(1 - x) = \frac{5\bar{F} - 1}{4} \quad (55)$$

to estimate error parameters p and q , where \bar{F} is the reported average two-qubit gate fidelity in the experiment.

C Error parameters used in simulations

In this section, we provide a comprehensive overview of the parameters utilised within our virtual devices. This is intended to enable a precise reproduction of the simulations detailed within this study.

The following points offer a general overview of the parameters we employed.

- Time is expressed in the unit of microseconds (μs), frequency is in the unit of megahertz (MHz), and distance is expressed in micrometres (μm), by default, unless stated otherwise; e.g., see the case of NV-center.
- Gate fidelity of parameterised gates is assumed to be obtained via a randomised benchmarking method.
- When T_2 is used, we assume some Hahn-echo or dynamical-decoupling sequences are implicitly applied to or integrated into the subsequent pulses of the passive qubits.
- In practice, the severity of noise has a complex relation to the obtained gate, e.g., X vs \sqrt{X} . We approximate this by the parameter angle; namely, given the error parameter ε and gate parameter θ , the used error parameter is scaled to $\tilde{\varepsilon} := \varepsilon \frac{|\theta|}{\pi}$, where $\tilde{\varepsilon}$ should be in the proper range, e.g., $\tilde{\varepsilon} \in [0, \frac{1}{2}]$ for single-qubit dephasing noise parameter. Such an approximation applies unless stated otherwise, e.g., in the case of superconducting qubits gate duration is identical regardless of the gate parameter.

Table 1: Variables used within the virtual two-node ion traps on the entanglement distillation. Here we assume every ion is identical on both nodes.

Variable	Value	Description
Nodes	{(Alice,4), (Bob,4)}	The number of ions on each specified node.
T1	3×10^9	T_1 value of each qubit.
T2s	10×10^5	T_2^* value of each qubit.
StdPassiveNoise	True	Apply the standard free-induction T_1 and T_2^* decay on passive qubits.
DurMove	{shuttling:25, split:50, combine:50, swap location:10}	Duration for each moves.
FidInit	0.9999	Fidelity of the simultaneous ions initialisation in a zone.
DurInit	20	Duration of the simultaneous ions initialisation in a zone.
DurRead	50	Duration of a single ion readout.
BFProb	0.001	Probability of bit-flip error in the readout process.
FidSingleXY	0.99999	Gate fidelity of the single-qubit x - and y - rotations.
EFSingleXY	1:0	Error ratio <i>depolarising:dephasing</i> when applying single-qubit x and y rotations.
RabiFreq	10	The average Rabi frequency of single-qubit gates.
FreqCZ	0.1	Gate frequency in implementing CZ gate.
FidCZ	0.999	Gate fidelity of CZ operator.
EFCZ	0.1:0.9	Error ratio <i>depolarising:dephasing</i> when applying CZ gate.
FreqEnt	0.1	Frequency of successful remote Bell pair generation.
FidEnt	0.95	Fidelity of the generated remote Bell pair.
EFEnt	0.1:0.9	Error ratio <i>depolarising:dephasing</i> when obtaining the remote Bell pair.

Table 2: Variables used in the virtual NV-center diamond qubits on the simulating the dynamics of a BCS model. The following setting corresponds to the NV-center with five qubits $\{q_0, \dots, q_4\}$, where q_0 indicates the NV^- electron spin and the other $\{q_1, \dots, q_4\}$ correspond to the nuclear ^{13}C spin. Time is expressed in seconds (s) and frequency is expressed in Hertz (Hz).

Variable	Value	Description
QubitNum	5	The number of physical active qubits for computations.
T1	{3600, 60, 60, 60, 60}	T_1 values of qubits $\{q_0, \dots, q_4\}$, respectively.
T2	{1.5, 10, 10, 10, 9}	T_2 values of qubits $\{q_0, \dots, q_4\}$, respectively.
FreqWeakZZ	3	The frequency of weak ZZ -coupling among nuclear spin qubits, on passive qubits.
FreqSingleXY	{15000, 0.5, 0.5, 0.5, 0.5} $\times 10^3$	Rabi frequencies of the single-qubit x - and y - rotations on qubits $\{q_0, \dots, q_4\}$, respectively.
FreqSingleZ	{32, 0.4, 0.4, 0.4, 0.4} $\times 10^6$	Rabi frequencies for the single z -rotation on qubits $\{q_0, \dots, q_4\}$, respectively.
FreqCRot	{1.5, 2.8, 0.8, 2} $\times 10^3$	Frequency of conditional rotations $CRx^\pm(\theta)$ and $CRy^\pm(\theta)$ on nuclear spins $\{q_1, \dots, q_4\}$, respectively, conditioned on the electron spin state.
FidCRot	{0.98, 0.98, 0.98, 0.98}	Fidelity of conditional rotations $CRx^\pm(\theta)$ and $CRy^\pm(\theta)$ on nuclear spins $\{q_1, \dots, q_4\}$, respectively, conditioned on the electron spin state.
FidSingleXY	{0.9995, 0.995, 0.995, 0.99, 0.99}	Gate fidelity of single Rx and Ry rotations on qubits $\{q_0, \dots, q_4\}$, respectively.
FidSingleZ	{1, 1, 1, 1, 1}	Fidelity of single Rz rotation on each qubit obtained by random benchmarking.
EFSingleXY	0.75:0.25	Error ratio <i>depolarising:dephasing</i> when applying single-qubit x and y rotations.
EFCRot	0.9:0.1	Error ratio <i>depolarising:dephasing</i> when applying conditional rotations CRx^\pm and CRy^\pm .
FidInit	0.999	Fidelity of direct initialisation, namely initialising electron spin qubit q_0 .
DurInit	2×10^{-3}	Duration of direct qubit initialisation on the electron spin qubit q_0 .
FidMeas	0.946	Fidelity of direct qubit measurement on the electron spin qubit q_0 .
DurMeas	2×10^{-5}	Duration of direct qubit measurement on the electron spin qubit q_0 .

Table 3: Variables used within the virtual (Rydberg) neutral atoms to simulate stabiliser measurements on a 1D cluster and a logical Steane code states. We assume every atom has identical characteristics.

Variable	Value	Description
T2	100×10^6	The T_2 value of each atom.
VacLifeTime	100×10^6	Vacuum life time of each tweezer, before the atom lost to the environment.
RabiFreq	0.1	Rabi frequency for single-qubit operators.
UnitLattice	3	The unit length used in atom coordinates. This also a key to access internal parameter of the virtual device.
BlockadeRadius	1	Short-range dipole-dipole interaction of Rydberg atoms; this becomes the maximal distance requirement among atoms that implement multi-qubit gate operations.
ProbLeakInit	0.01	Leakage probability in the atom initialisation, where some population is excited outside the computational basis.
DurInit	5×10^5	Duration of qubit initialisation that happens in the beginning. This involves atom loading and characterising.
FidMeas	0.975	Fidelity of qubit measurement.
DurMeas	10	Duration of qubit readout.
ProbLossMeas	0.0001	Probability of atom loss out of the optical trap during measurement process.
1D cluster state simulation		
QubitNum	12	The number of atoms or qubits for computations.
AtomLocations	$\{(0,0), (1,0), (2,0), (3,0), (4,0), (5,0), (6,0), (7,0), (8,0), (9,0), (10,0), (11,0)\}$	Initial (2D) coordinate of physical locations of atoms $\{q_0, \dots, q_{11}\}$, accordingly.
ProbLeakCZ	$\alpha = 0.02, \beta = 0.0001$	Leakage probability in executing (multi) controlled-Z; these values correspond to the parameter in the CPTN map given in Equation (28).
ProbBFRot	$p(1 \rightarrow 0) = 0.001,$ $p(1 \rightarrow 0) = 0.03$	Probability of asymmetric bit-flip error during single rotation operation.
Logical state of Steane code simulation		
QubitNum	7	The number of atoms or qubits for computations.
AtomLocations	$\{(0, 1), (1, 1), (2, 1), (4, 1), (2, 0), (4, 0), (5, 0)\}$	Initial (2D) coordinate of physical locations of atoms $\{q_0, \dots, q_8\}$, accordingly.
ProbLeakCZ	$\alpha = 0.11, \beta = 0.0001$	Leakage probability in executing (multi) controlled-Z; these values correspond to the parameter in the CPTN map given in Equation (28).
ProbBFRot	$p(1 \rightarrow 0) = 0.1,$ $p(1 \rightarrow 0) = 0.0001$	Probability of asymmetric bit-flip error during single rotation operation.

Table 4: Variables used within the virtual silicon qubits device on the simulation of Bell pairs generation.

Variable	Value	Description
QubitNum	6	The number of physical active qubits for computations.
T1	10^4	T_1 duration of each qubit.
T2	{14, 21.1, 40.1, 37.2, 44.7, 26.7}	T_2 duration of qubits $\{Q1, \dots, Q6\}$, respectively.
QubitFreq	{15.62, 15.88, 16.3, 16.1, 15.9, 15.69} $\times 10^3$	The fundamental qubit frequency of qubits $\{Q1, \dots, Q6\}$
RabiFreq	{5, 5, 5, 5, 5, 5}	The Rabi frequency of single-qubit x and y rotations for qubits $\{Q1, \dots, Q6\}$, respectively.
OffResonantRabi	True	Apply off-resonant driving noise when applying single qubit rotations.
StdPassiveNoise	True	Apply the standard free-induction T_1 and T_2 decay on passive qubits.
FidSingleXY	{0.9977, 0.9987, 0.9996, 0.9988, 0.9991, 0.9989}	Fidelities of single-qubit x and y rotations when applied to qubits $\{Q1, \dots, Q6\}$, respectively.
EFSingleXY	0:1	Error ratio <i>depolarising:dephasing</i> when applying single-qubit x and y rotations.
FreqCZ	{12.1, 11.1, 6.6, 9.8, 5.4}	Rabi frequency of controlled- Z or $-Ph(\pi)$ gate when operated on qubit pairs $\{(Q1, Q2), \dots, (Q5, Q6)\}$, respectively.
FidCZ	{0.937, 0.934, 0.929, 0.997, 0.979}	Fidelity of controlled- Z or $-Ph(\pi)$ gate when operated on qubit pairs $\{(Q1, Q2), \dots, (Q5, Q6)\}$, respectively.
EFCZ	0:1	Error ratio <i>depolarising:dephasing</i> on the two-qubit gates error.
ExchangeRotOn	$\begin{pmatrix} 0 & 0.023 & 0.018 & 0.03 & 0.04 \\ 0.05 & 0 & 0.03 & 0.03 & 0.04 \\ 0.05 & 0.03 & 0 & 0.07 & 0.042 \\ 0.038 & 0.03 & 0.031 & 0 & 0.25 \\ 0.033 & 0.03 & 0.02 & 0.03 & 0 \end{pmatrix}$	Cross-talk on the passive qubits in form of entangling rotation controlled- $Rz(\delta_{i,j}\frac{\theta}{\pi})$, where $\delta_{i,j}$ is the matrix element and θ is the angle of the gate; this applies when a two-qubit gate is active.
ExchangeRotOff	{0.039, 0.015, 0.03, 0.02, 0.028}	Cross-talk on the passive qubits in form of entangling rotation controlled- $Rz(\alpha_{i,i+1})$, where $\alpha_{i,i+1}$ is specified here; this applies when no two-qubit gate is active.
FidRead	0.99	Fidelity of the parity readout on the edges, between qubits $Q1, Q2$ and $Q5, Q6$.
DurRead	10	The total duration on the parity readout on the edge qubits: $Q1, Q2$ and $Q5, Q6$.

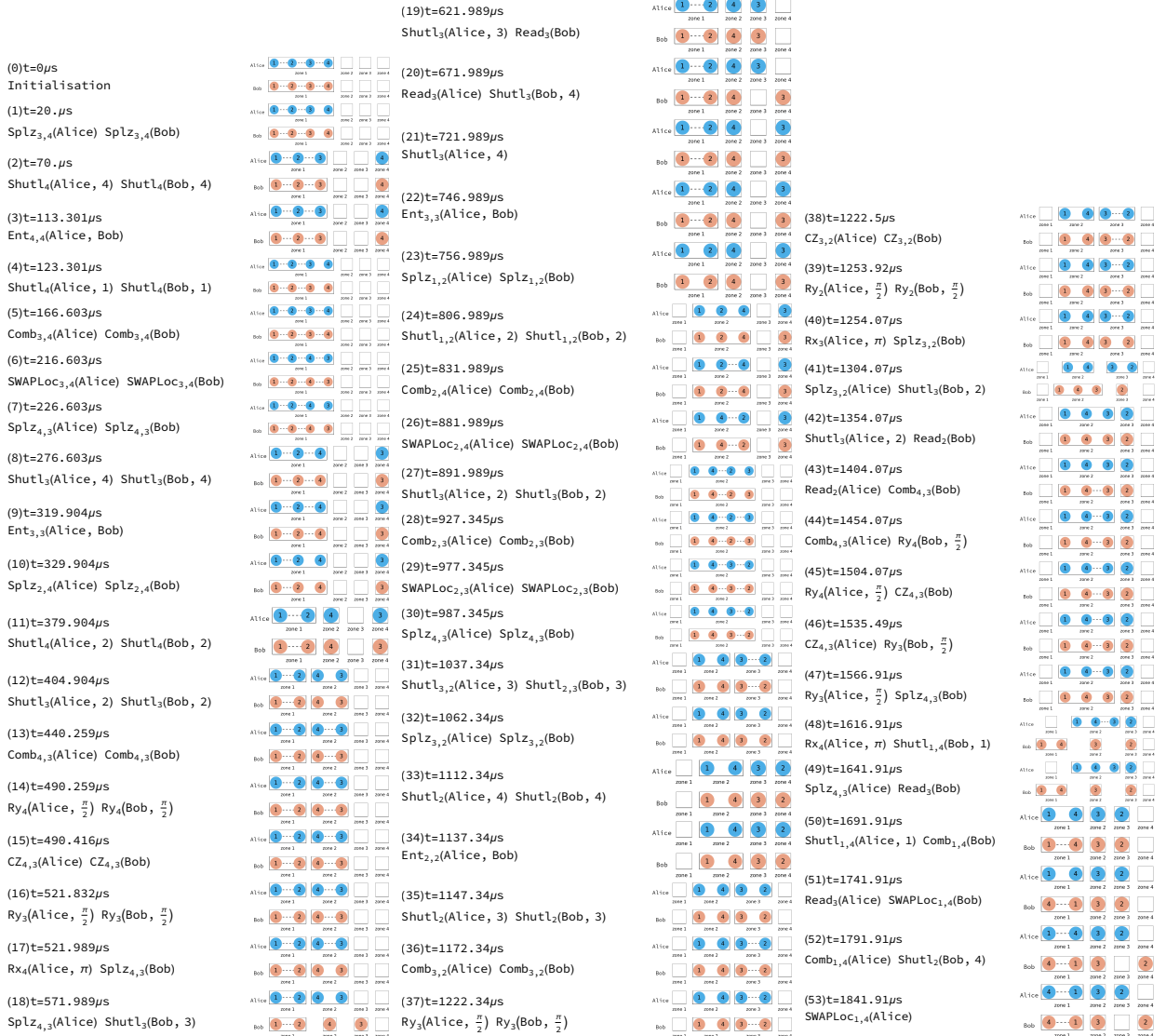
Table 5: Variables used within the virtual superconducting qubits to simulate a variational quantum eigensolver to approximate the ground state of a hydrogen molecule.

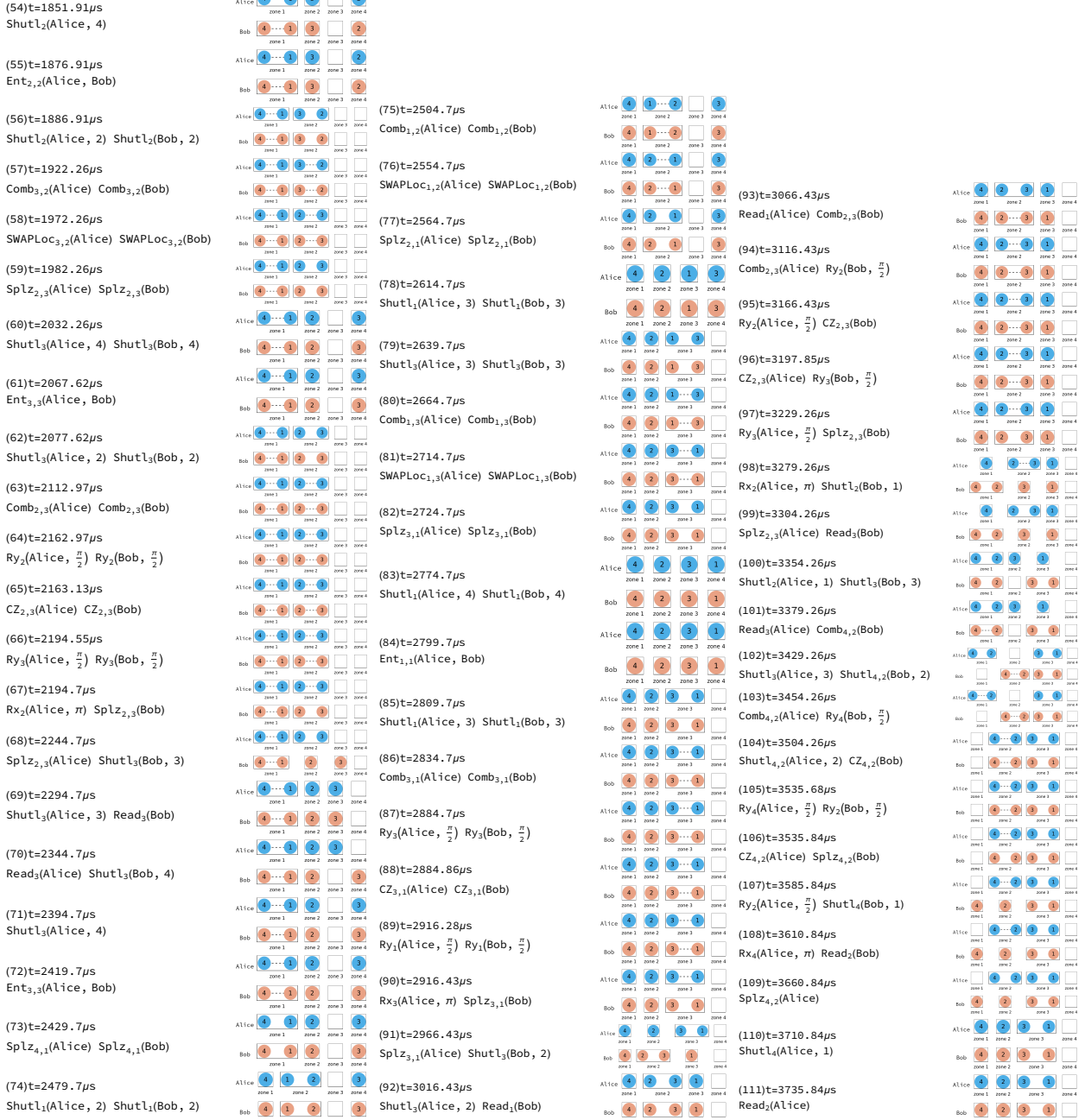
Variable	Value	Description
QubitNum	6	The number of physical active qubits for computations.
T1	{63, 93, 109, 115, 68, 125}	T_1 values of qubits $\{Q_0, \dots, Q_5\}$, respectively.
T2	{113, 149, 185, 161, 122, 200}	T_2 values of qubits $\{Q_0, \dots, Q_5\}$, respectively.
ExcitedInit	{3.2, 2.1, 0.8, 0.9, 2.5, 0.7} $\times 10^{-2}$	The probability of the excited population from the ground state (p_j) for qubits $\{Q_0, \dots, Q_5\}$, respectively. The qubits will be initialised into statistical mixture of $\bigotimes_j (p_j 1\rangle\langle 1 + (1 - p_j) 0\rangle\langle 0)$.
QubitFreq	{4.5, 4.9, 4.7, 5.1, 4.9, 5.3} $\times 10^3$	The fundamental qubit frequency of qubits $\{Q_0, \dots, Q_5\}$, respectively.
ExchangeCoupling	{(0,1):4, (0,2):1.5, (1,3):1.5, (2,3):4, (2,4):1.5, (3,5):1.5, (4,5):4}	The capacitive coupling strength constants that allows exchange interaction between two transmons (Q_i, Q_j) but it creates residual cross-talks on passive noise; thus, it has the form of ZZ interaction. The cross-talk can be mitigated by tuning the interactions accordingly, i.e., when operating a siZZle gate; thus, if a siZZle gate is on, the ZZ cross-talk is gone.
Anharmonicity	{296.7, 298.6, 297.4, 298.3, 297.2, 299.1}	The anharmonicity frequency of qubits $\{Q_0, \dots, Q_5\}$, respectively. In this model, it shifts the strength of the static ZZ cross-talk.
FidRead	{0.9, 0.92, 0.96, 0.97, 0.93, 0.97}	Readout fidelity of qubits $\{Q_0, \dots, Q_5\}$, respectively.
DurMeas	5	Duration of qubit readout, taking into account (classical) outputs classification process.
DurRxRy	0.05	Gate duration to implement single-qubit rotations $Rx(\theta)$ and $Ry(\theta)$, that remains constant regardless θ .
DurZX	0.5	Gate duration to implement cross-resonance gates ZX .
DurZZ	0.5	Gate duration to implement siZZle gates
StdPassiveNoise	True	Apply the standard passive noise, namely the free-induction T_1 - and T_2 -decays.
ZZPassiveNoise	True	Apply the static ZZ interaction passive noise.

D Entanglement distillation on trapped ions

The following figures show every sequence to perform three rounds of phase-flip error entanglement distillation. The left side shows the time and the operator performed at that time. The left side shows arrangement of the ions after applying the operator on the left side.

Figure 19: Operations and moves involved in three rounds of phase-flip distillation on the virtual trapped ions which comprises 112 sequences.





E Parallelisation in Neutral Atoms

Parallelism of quantum gates in neutral atoms is subject to the Rydberg blockade mechanism. As illustrated in Figure 12, gate parallelism is permitted for the qubits outside the restricted zone, i.e., the resulting zone from the interacting atoms. Note that the end user is responsible for reconfiguring the register to accommodate such a blockade mechanism.

In the following example, we have an array of 9 atoms in a square lattice with distance d , where each atom has blockade radii $r_b = \sqrt{2}d$. The first configuration is shown in Figure 19 panels A-C, which is then reconfigured by shifting a column of atoms, as shown in Figure 19 panels D-F.

For a concrete example, We show the parallelism of a circuit comprises the following operations:

1. Initialise the quantum register: $\{Init_j\}$
2. Apply Hadamard gates to all atoms: $\{H_j\}$

3. Apply a three-qubit gate: $C_3[Z_{6,7}]$
4. Shift location of atoms 0, 1, and 2 horizontally: $\text{ShiftLoc}_{0,1,2}[\{-x, 0\}]$
5. Apply three-qubit gates: $CZ_{0,1,3}CZ_{5,7,8}$
6. Do nothing: Wait
7. Apply Hadamard gates to all atoms: $\{H_j\}$.

The tool will schedule the circuit shown in [Figure 19](#) due to the blockade restrictions.

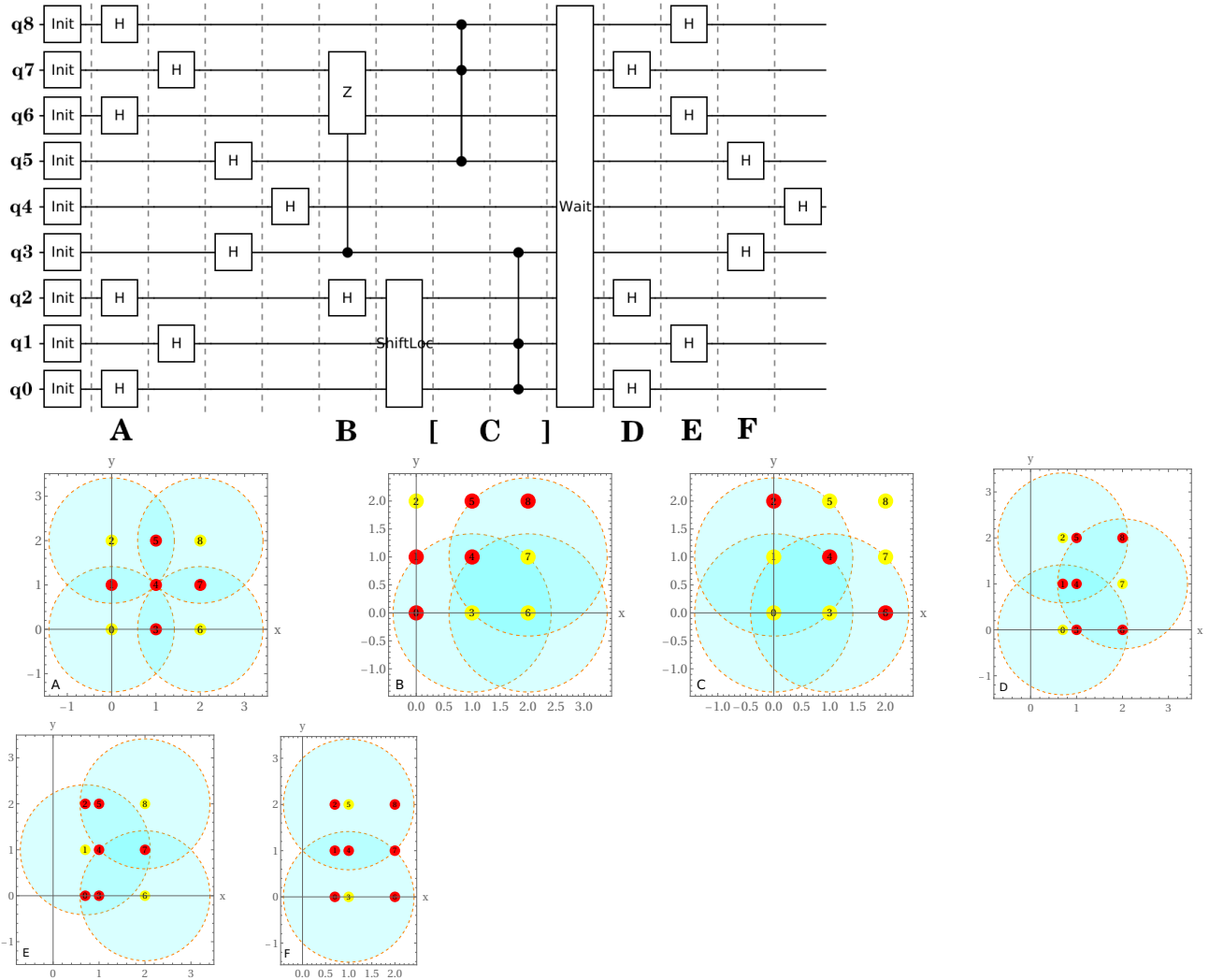


Figure 19: In the circuit, qubit q_j represents atom j in panels A-F. The yellow atoms indicate active qubits, i.e., a quantum operation is acted upon. All initialisation is done in parallel, which represents loading the atoms or preparing the register. At column **A**, Hadamard gates H_0, H_2, H_6, H_8 are applied simultaneously because, as Panel A illustrates, yellow atoms 0, 2, 6, 8 are not within each other's interaction zones—unlike the red atoms. In column **B**, gate parallelization is feasible for a three-qubit gate acting on atoms 3, 6, 7, along with a Hadamard H_2 ; this is viable because atom 2 is outside the restricted zone, as depicted in panel B. Here, we assume operations that reconfigure the register, such as ShiftLoc and SWAPLoc , are executed serially: no concurrent operations are permitted. Columns in **C** demonstrate that the two 3-qubit gates cannot be implemented simultaneously, as panel C indicates atoms 5 and 7 are within the restricted zone when the 3-qubit gate involving atoms 0, 1, 3 is activated. Following the reconfiguration of atoms as per panel D, the arrangement of Hadamard gates in column **D** differs from that in column **A**: the proximity of more atoms reduces the number of gates that can be parallelized. This principle also applies to columns **E** and **F**, corresponding to panels E and F, respectively.